To:

Ms. Patricia Poire

Executive Director

Kern Groundwater Authority

1800 30th Street, Suite 280

Bakersfield, CA 93301

From:

D. W. Vasco

Lawrence Berkeley National Laboratory

Energy Geosciences Division, Building 74

Berkeley, CA 94720

dwvasco@lbl.gov

1. Background and Purpose

Data gaps related to understanding the causes and magnitude of subsidence in the Kern County Subbasin (KCS) (Figure 1.1) have been identified by the KCS. Addressing these gaps are necessary for establishing science-based Measurable Objectives and Maximum Thresholds (MOs/MTs) for land subsidence in the KCS, and future sustainability planning, particularly as it relates to critical regional infrastructure such as the California Aqueduct (Aqueduct) and the Friant-Kern Canal (Canal).

This current study builds upon a July 2022 report completed by Lawrence Berkeley National Laboratory (LBNL) on behalf of the members of the KCS by utilizing findings and conclusion from the 2022 study as a point of departure for further exploration of the causes and magnitude of subsidence in the KCS. The current study also integrates findings from, among other sources, previous Differential Interferometric Synthetic Aperture Radar (DInSAR) studies conducted by Earth Consultants International (ECI) prepared on behalf of the Kern Groundwater Authority (KGA) and the KCS. To provide context, this report provides a synopsis of the LBNL 2022 study followed by a broader look at subsidence in the California Central Valley and then applies those findings and conclusions to conditions and data gaps observed in the KCS.
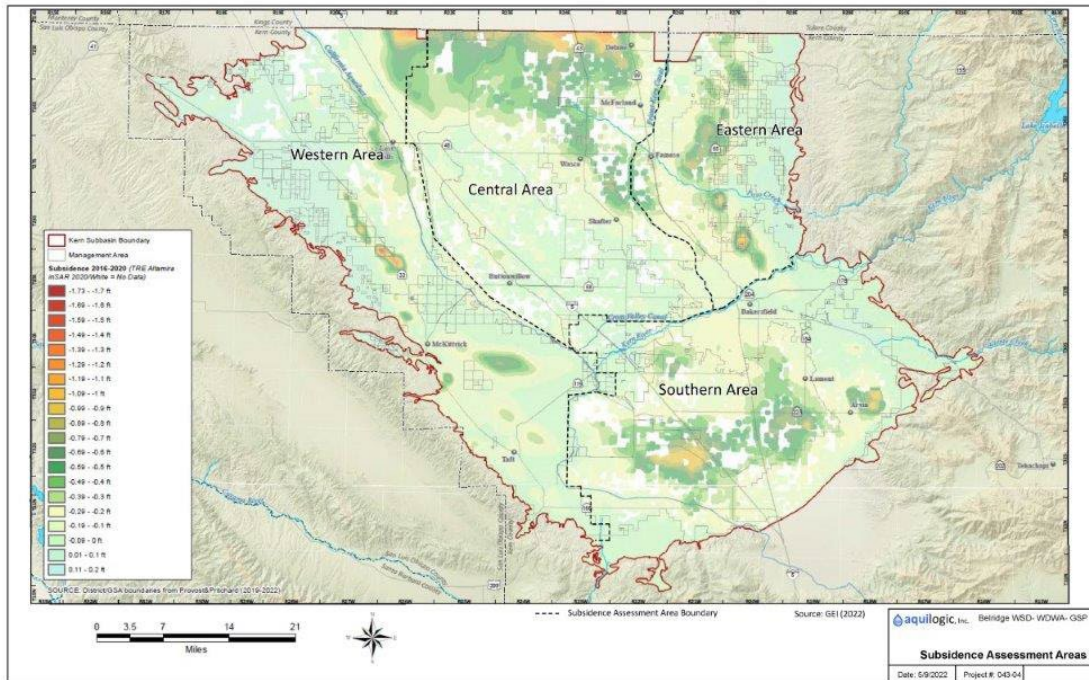

Figure 1.1. Outline of the Kern County Subbasin (KCS) and the four sub-areas used in the analysis. The color variations indicate subsidence within the subbasin, with warmer colors indicating greater subsidence.

2022 Study

In July 2022, LBNL conducted a subsidence study on behalf of the member agencies of the KCS. The study was undertaken in response to requirements of the California Sustainable Groundwater Management Act (SGMA), which has identified land subsidence induced by groundwater pumping as an undesirable result. SGMA-related sources of pumping and associated groundwater use in the KCS include municipal, agricultural, and industry. It is important to note that oil and gas extraction activities, which generate a significant volume of "produced water" in the KCS, are SGMA exempt. The purpose of the 2022 study was to determine the baseline rate of subsidence in the KCS for the period between 2015 and 2021. The study data were also compared the March 2021 Differential Interferometric Synthetic Aperture Radar (DInSAR) Study conducted by Earth Consultants International (ECI) on behalf of the Kern Groundwater Authority (KGA) and other Groundwater Sustainability Agencies (GSAs) in the KCS. The objectives of the July 2022 study were to highlight the temporal and spatial variation in subsidence rates and distinguish variations in rates between the differing sub-domains present in the KCS. Critical regional infrastructure vulnerable to deleterious effects caused by land subsidence in the KCS are the California Aqueduct (Aqueduct) and the Friant-Kern Canal (Canal). To facilitate the assessment and discussion of the data in the 2022 study, the KCS was subdivided geographically into four regions, Eastern, Central, Western and Southern (Figure 1.1).
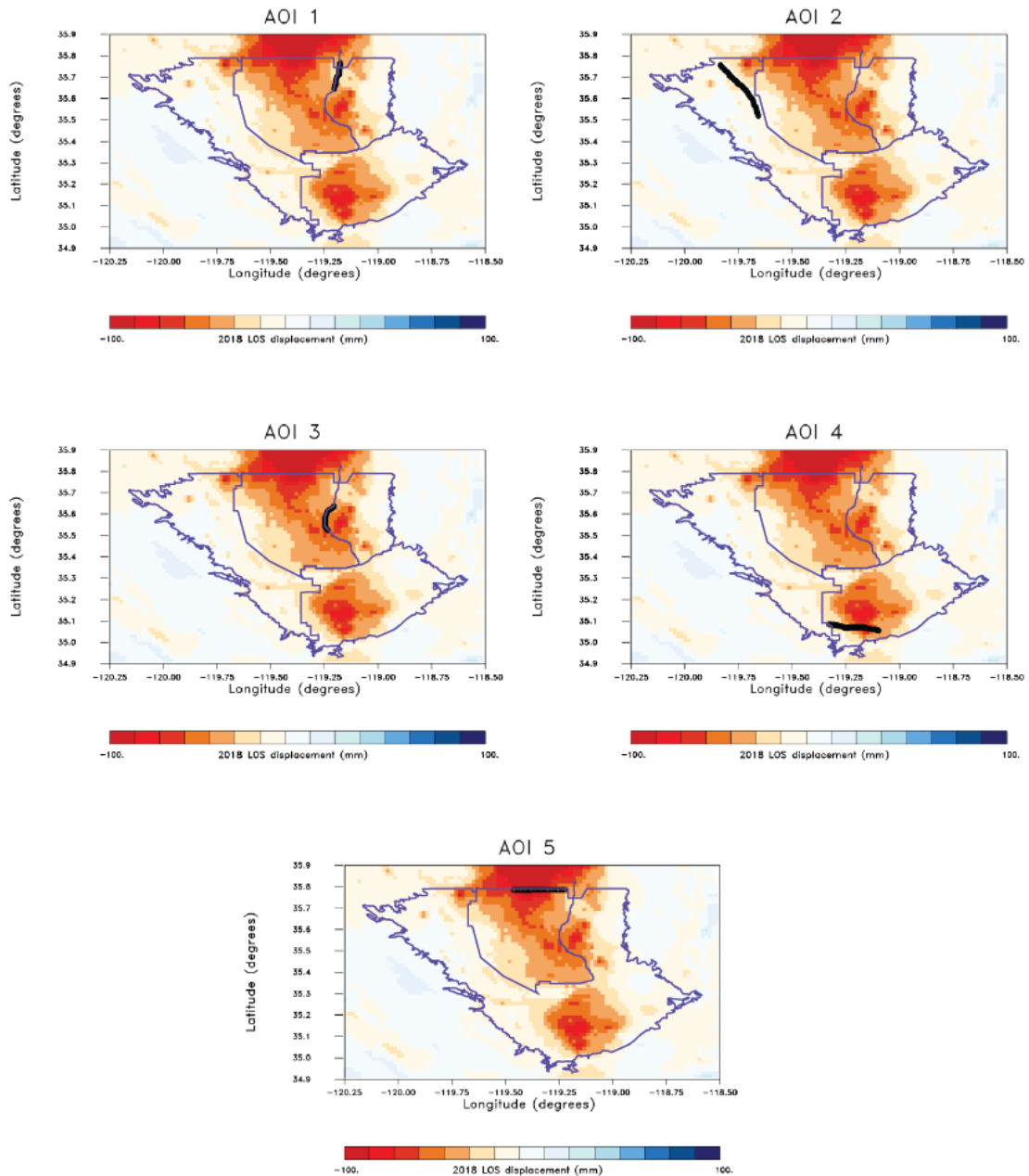
Figure 1.2. The five areas of interest (AOI) of the KCS that will be discussed in this report. The thick line indicates the points comprising each AOI while the color scale indicates the background line-of-sight (LOS) displacement field for the water year 2018 in milli-meters.

Within these geographic regions the KCS identified five areas of interest (AOIs) that required further study due to their particular sensitivity to subsidence (Figure 1.2):

1. AOI 1: Friant-Kern Canal MP 120-130 (Eastern Region)
2. AOI 2: LHOF Aqueduct MP 195-215 (Western Region)
3. AOI 3: Friant Kern Canal MP130-137 (Eastern Region)
4. AOI 4: Aqueduct MP 264-271 (Southern Region)
5. AOI 5: Northern boundary of Kern County (Central Region)

Some key conclusions and recommendations of the 2022 LBNL report were:

1. Surface deformation in the KCS is a complex and dynamic process. Factors to be considered are isostatic loading, natural consolidation of soils, soil types, oil extraction, groundwater pumping and tectonic activity, among others.

2. These processes operate on differing time scales whereby some processes are elastic and produce near instantaneous responses while other processes might be best be described as visco-elastic, poro-elastic, or simply inelastic. Thus, deformation over short time intervals may still be influenced by events that are much earlier.

3. The main drivers for much of the deformation (either subsidence and/or uplift) in the KCS are agricultural groundwater pumping and non-SGMA-related activities. Managed banking of surface water has not caused SGMA undesirable results (e.g., inelastic subsidence induced by groundwater extraction).

4. The spatial distribution of surface displacement, and hence subsidence, is highly variable and typically concentrated within the various sub-areas. This concentration is most notable for oil and gas fields, especially in western Kern County.

5. The large-scale (spatial) rates indicate a background "floor" of subsidence values in the KCS of around -1.0 cm/year (-0.4 inches/year) for the eastern, western, and southern regions, interrupted by decreases in subsidence in non-oilfield areas during wetter years leading to net uplift.

6. The Central Region, with its greater exposure to the large-scale subsidence bowl originating to the north of the KCS, has a larger average background rate that is higher, around -1.6 cm/year (-0.65 inches/year).

7. The large and widespread subsidence to the north of the KCS and mainly in the Central Region is due to agricultural water withdrawal. Smaller scale subsidence in the Western and Eastern Regions is primarily due to oil and gas extraction and is of a different character from the agricultural-related subsidence both spatially and temporally.

8. Data indicates that the subsidence rate in the KCS has increased since 2020, most dramatically in the Central Region located adjacent to the subsidence bowl originating to the north of the KCS near the towns of Corcoran and Alpaugh.

9. The annual subsidence rates of approximately -8.1 cm, -6.6 cm and -6.0 cm/year (-3.2, -2.6, and -2.4 inches/year) respectively for the Central, Southern, and Eastern Regions are in line with estimates in the March 2021 report by ECI, who found subsidence rates of -5.0 to -7.6 cm/year (-2 to -3 inches/year) in the northern

edge of the Kern County Subbasin and -7.6 to -10.16 cm/year (-3 to -4 inches/year) south of Bakersfield. In the Western Region there is an anomalously high value of -19.5 cm/year (-7.7 inches/year). This area, located northeast of the Aqueduct, may be related to the subsidence bowl located to the north of Kern County, but requires further study to ascertain a probable cause. Outside of this anomalous area, the western sub-domain has a relatively moderate mean subsidence rate (approximately -1 cm/year (-0.4 inches/year) in 2020, though there are higher rates of subsidence associated with some oil and gas fields.

10. The Interferometric Synthetic Aperture Radar (InSAR) line-of-sight (LOS) displacements are dominated by subsidence but there will also be notable horizontal displacement, particularly from the subsidence bowl at the northern edge of the subbasin. Such north-south and east-west displacements can be estimated from an inversion for volume change (least squares fitting), as in Vasco et al. (2019), followed by a forward geomechanical calculation of the three-dimensional displacements based upon the estimated volume change. Such displacements require further study and validation, particularly as they relate to critical regional infrastructure.

Subsequent additional studies proposed by the LBL in 2022 included:

- Installation of new land-based geodetic technology (e.g., GPS stations, extensometers etc.) to further assess the causes, extent and magnitude of KCS subsidence,
- A review of the recent Stanford University subsidence model, a review of Central Valley Aerial Electro-magnetic (AEM) data,
- An integrated review of Gravity and Climate Change Experiment (GRACE) data, well water level observations, along with existing KCS GPS elevation and InSAR data.

2. Current Study

California Central Valley

This current follow-up study was undertaken to refine the baseline rate of subsidence in the KCS for the study period of 2015 to 2021. Study data was also compared to The March 2021 DInSAR Study conducted by ECI on behalf of the Kern Groundwater Authority (KGA) and other Groundwater Sustainability Agencies (GSAs) in the KCS. The publicly available JPL database was utilized for this study.

For comparison, and to understand yearly variations, the cumulative line-of-sight displacement and the yearly displacement rates were determined for a roughly seven-year period extending from early 2015 until late 2021. These values were used to better assess the vulnerability of critical infrastructure within the subbasin. Regional

critical infrastructure identified by the KCS include the Canal, located along the eastern side of the KCS, and the California Aqueduct (Aqueduct), which follows a course along the western side of the KCS. The region is sub-divided into four regions based primarily on geography, hydrogeology, and current general land use (Figure 1.1).

The Eastern Region is bounded on the west by the Friant-Kern Canal and on the east by the foothills of the Sierra-Nevada Range. The Eastern Region hosts both agricultural and some oil field activities. Groundwater quality is generally good in the Eastern Region and is utilized for various SGMA-related purposes (e.g., municipal, agriculture, industry). Deliveries of surface water via the Canal are an important source of water for agriculture in the KCS, although not all growers in the Eastern Region have access to the Canal water.

The Central Region of the KCS is characterized by widespread agricultural activity, interspersed with municipal and industrial uses. Scattered oilfield operations are also present. The Central Region is particularly susceptible to land subsidence induced by groundwater extraction (e.g., agricultural activity). This is due to the presence of an extensive layer of impermeable clay, the Corcoran Clay, that defines the top of a confined regional aquifer. Groundwater withdrawal from the confined aquifer, and the resulting fluid pressure decrease, leads to compaction of any layers of fine-grained sediments there. To the north of the Central Region, outside of the KCS's official boundary, there is a large subsidence bowl centered near the towns of Corcoran and Alpaugh, California. Subsidence associated with this northern bowl is documented in the KCS. The Central Region has undergone the most significant subsidence in the KCS, and it is important to understand the factors that contribute to this subsidence. Subsidence in the north is primarily driven by the activity that is outside of the KGA boundary. However, it does have a major impact on the KGA, and for this reason the member GSAs of the KCS have undertaken a comprehensive survey of the larger San Joaquin basin, of which the KCS is a part, to better understand the main drivers of subsidence in the southern San Joaquin basin.

 The Western Region of the KCS is distinguished by extensive areas of open rangeland and oilfield operations, interspersed with some cultivated lands. The Western Region is bordered by the Temblor range to the west. Along its eastern boundary are a series of roughly north-south oriented anticlines. These geologic folds, which act as impediments to groundwater recharge flow towards the axis of the basin, have been the site of oilfield activities since the early 20th Century. Much of the Western Region has no significant current or planned groundwater use because of naturally poor water quality due to the presence of marine sediments and saline connate water. As such, surface water deliveries via the Aqueduct are the primary source of agricultural water. Still, some groundwater is used for blending when Aqueduct deliveries are scarce. Significant volumes of oilfield "produced water," typically containing high concentrations of total dissolved solids (TDS), are generated in the Western Region. Produced water is an entrained by-product of oil production common to almost all oilfields in the KCS. Oil on the west side is produced from some of the same aquifers used by agriculture in the KCS (e.g.,

Tulare, Etchegoin Formations). Produced water is exempt from SGMA, and therefore outside of the control of either the KGA or the KCS.

The Southern Region is characterized by a mixture of land uses including agriculture, urban development and some oilfield operations. SGMA-related groundwater extractions include industrial, municipal and agriculture. The Southern Region also receives surface water deliveries from the California Aqueduct as well as other intra-KCS conveyance infrastructure.

2. Review of the Recent Stanford Model and AEM Studies.

It is long been known that the one of the primary drivers of subsidence in the Central Valley of California (Valley) is inelastic deformation in the fine-grained sediments, largely due to dewatering-induced irreversible grain re-arrangement, leading to permanent deformation (Meade 1964, Ireland et al. 1984). To date, it has proven difficult to fully quantify these effects, due to uncertainty regarding the physical distribution, thickness, and composition of the Valley clay layers. A quantitative model was advanced by Helm (1975, 1976) based upon the diffusion of pore pressure out of the clay layers, leading to inelastic deformation due to the change in effective pressure. The result is a diffusion equation for effective stress that may be integrated numerically (Helm 1975, 1976). The methodology has been widely adopted and is still an area of active research (Lees et al. 2022). The diffusion of effective stress:

$$\sigma^e = \sigma - \rho g h$$

where σ is the overburden stress, ρ is the density of water, g is the gravitational acceleration, and h is the hydraulic head, is governed by the equation:

$$\frac{K_v}{S_s} \frac{\partial^2 \sigma^e}{\partial z^2} = \frac{\partial \sigma^e}{\partial t}$$

(Helm 1975, 1976, Smith et al. 2017, Smith and Knight 2019, Lees et al. 2022) where K_v is the vertical permeability, and S_s is the specific storage which is the sum of the skeletal specific storage S_{sk} and the storage due to the compressibility of the water, S_w,

$$S_s = S_{sk} + S_w.$$

The skeletal specific storage is a parameter that represents some extremely complicated physics involving both the elastic response of competent sediments, such as cemented sands and coarse-grained stable sediments, but also representing the behavior of highly deformable clays and clay rich silts. These types of sediments, which are

common towards the axis of the subbasin (i.e., Central Region) at depths above 400 m (1,312 ft), typically have lower permeability and act as aquitards, barriers to flow, (Helm 1975, 1976). The large inelastic deformations are assumed to be driven by particle re-arrangement in the clay aquitards of varying thicknesses (Meade 1964). Meade has also noted the complicated chemistry and mineralogical effects that can impact clay deformation. Below 400 m (1,312 ft), coarse sediments dominate the center of the San Joaquin Valley basin.

One aspect of this theory that has not been examined in detail is the assumption that the vertical permeability is constant during and after the deformation of the clays. It is quite likely that the particle re-arrangement will reduce the vertical permeability considerably, and this reduction in permeability may act to isolate the interior of thick clay layers from the permeable coarse sediments that bound it. Thus, further dewatering of the interior of the clay layer by effective pressure changes in the surrounding coarse sediments might be retarded and reduced. This is a topic that could have implications for both the temporal behavior of long-term inelastic deformation and the ultimate amount of water that is available for extraction from the Central Valley aquifers.

The dramatically different behavior of coarse clastic sediments and fine grained, clay-bearing layers points to the importance of mapping the different sediment types throughout California's Central Valley. To date, the most comprehensive effort to map the textural variations in the Central Valley was the work done in support of the USGS Central Valley Hydrological Model (Faunt, 2009, Faunt et al. 2010). The USGS textural study was based upon the analysis of around 8,500 drillers logs to produce estimates of the percentage of coarse-grained sediments, or texture, from the surface to depths of 700 m (~2,296 feet) below the surface. The estimates were made for 15 m (~49 feet.) intervals and three-dimensional kriging was used to interpolate between wells in order to provide a grid of textural estimates (Faunt et al. 2010). The estimates can be used to map areas of predominantly coarse-grained and fine-grained sediments in the aquifers above and below the Corcoran Clay (Figure 2.1).
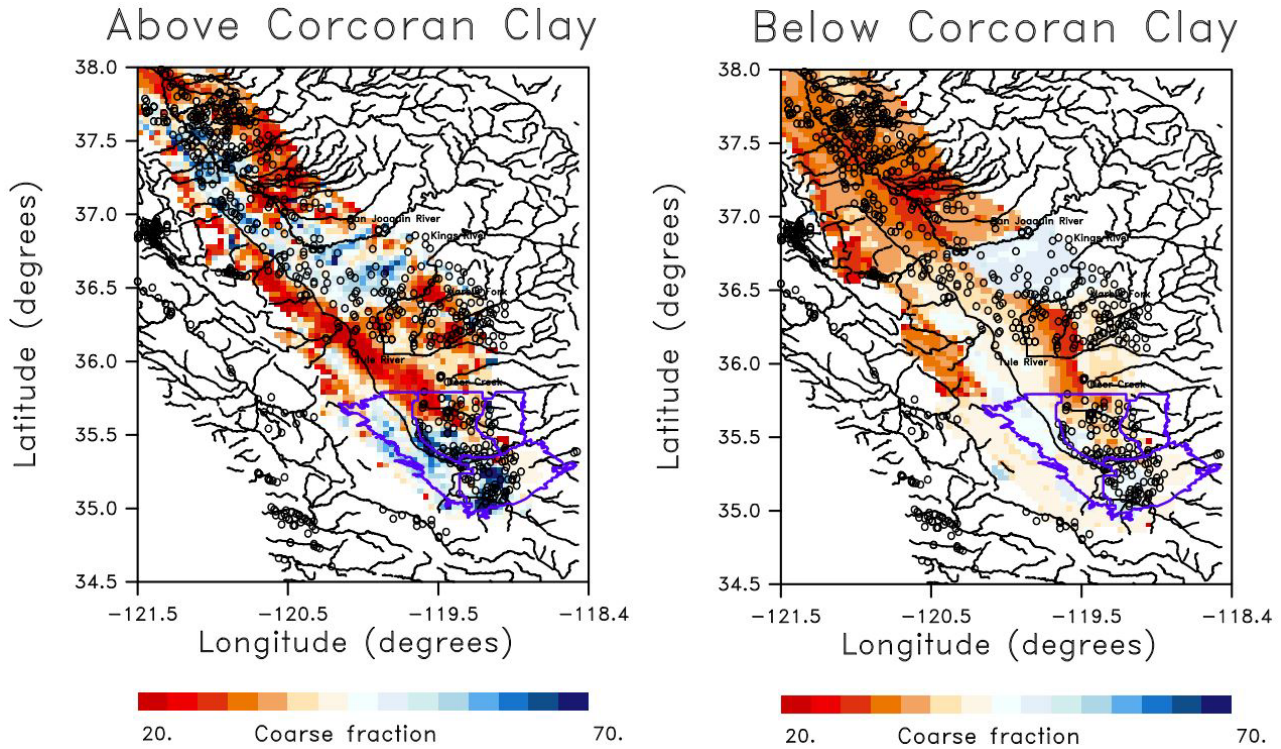
Figure 2.1. (Left) Coarse fraction averaged over the depth interval above the Corcoran Clay. (Right) Coarse fraction averaged over the depth interval below the Corcoran Clay.

Such maps were used to identify areas that are particularly susceptible to subsidence, those areas with predominantly fine-grained sediments lying below the Corcoran Clay. There are areas in the KCS where the Corcoran Clay is thin, discontinuous, or absent. Examples are the west side of the basin and the Kern fan.

The Stanford study by Lees et al. (2022) combined groundwater well data that were sensitive to changes in both the aquifer above the Corcoran Clay and changes in the deeper confined aquifer below the clay layer. The work was an attempt to extend the approach of Smith et al. (2017) for the estimation of the permanent loss of groundwater storage. In their study area a particularly long time series of groundwater head changes could be constructed by combining information for the available wells, resulting in observations from the 1950's through the end of 2021. A long time series is important because the time constant for inelastic deformation of a sediment sequence predict that inelastic deformation can continue for decades to centuries, though at greatly diminished rates. Specifically, the time constant, τ, depends upon the permeability of the clay layers, as well as their thicknesses according to the formula:

$$\tau = \frac{b^2 S_{sk}}{4K_v}$$

where b is the equivalent thickness obtained by summing over the thicknesses of all of the component clay layers:

$$b = \sqrt{\frac{1}{\Sigma_i\, n_i} \sum_i n_i\, t_i^2}$$

where the summation of over the n_i beds of thickness t_i. One of the difficulties in implementing this approach is obtaining detailed lithological information on thicknesses and clay contents of layers, as drillers logs may lack vital information.

For the study of Lees et al. (2022) generalized descriptions of the lithology were available from driller's logs, providing observations at each 5-foot depth interval but did not list clay interbeds. Resistivity logs were used to estimate the clay layers within the wells. There were some limitations in the sampling and most groundwater wells did not extend to the base of the aquifer. Thus, assumptions were made about the extent and fraction of clay below the wells. A model relating subsidence to groundwater head values, based upon Helm's formulation was used to relate head changes to surface deformation. This model was the basis for an inverse problem in which the surface deformation and groundwater head values were used to estimate the parameters of the model. Of the eight parameters, three of them, the density of water, ρ, the gravitational acceleration, g, and the specific storage of water, S_{sw}, which is related to the compressibility of water, are well known constants and may be fixed. Lees et al. (2022) neglect two other parameters, the elastic skeletal specific storage of both clays and water, assuming that they are negligible in comparison to the inelastic specific storage of clays, S_{skv}. This inelastic storage parameter and the vertical permeability, K_v, were the two critical unknowns that were solved for in the inverse problem. Lees et al. (2022) found that the solutions to the inverse problem were highly non-unique and that there were many tradeoffs between the parameters. The final range of time constants was 64 to 1,008 years. The model allowed them to estimate the distribution of compaction between the upper aquifer, the Corcoran Clay, and the lower aquifer. They found that approximately 6% to 11% of the subsidence could be attributed to the upper aquifer. The Stanford model can be used to calculate future subsidence but that will require estimates of the changes in hydraulic heads and effective pressure in the confined lower aquifer in order to be reliable. Thus, one will need to map precipitation into changes in hydraulic head and effective pressure in the lower aquifer, requiring an additional set of assumptions.

As may be seen in the equation for the time constant τ, the amount of inelastic deformation in a given time interval depends critically on knowledge of the distribution and thickness of clay layers below a given location at the Earth's surface. For the shorter intervals of a year or longer, the thin layers will be important, as they can be more numerous and will drain the fastest. The textural model of Faunt and co-workers (Faunt 2009, Faunt et al.

2010) provides the most direct information, as it is based upon drillers logs, however it only provides information over intervals of 15 m (49 feet) or more. An alternative approach is to infer the distribution of clay layers remotely, for example using electrical methods such as airborne electromagnetics (AEM). The possible resolution using this approach is 5 m (16.4 feet), however the depth of penetration is limited to the uppermost several hundred meters of the sediment column. Thus, sensitivity may not extend into the lower confined aquifer in the deeper portions of the basin. This is unfortunate, as the primary compaction occurs in the deeper confined aquifer and thus will depend upon the structure of the sediments.

Recent AEM work should improve the characterization of the lithology of the Central Valley above depths of a few hundred meters. At shallow depths the surveys generally provide resolution of clay layers 5 meters (16.4 feet) or greater in thickness. The recent AEM surveys are funded by the California Department of Water Resources (DWR) through a grant from Proposition 68. The entire Central Valley will eventually be covered by a series of AEM surveys. Surveys of selected basins completed to date have shown the value of such surveys in
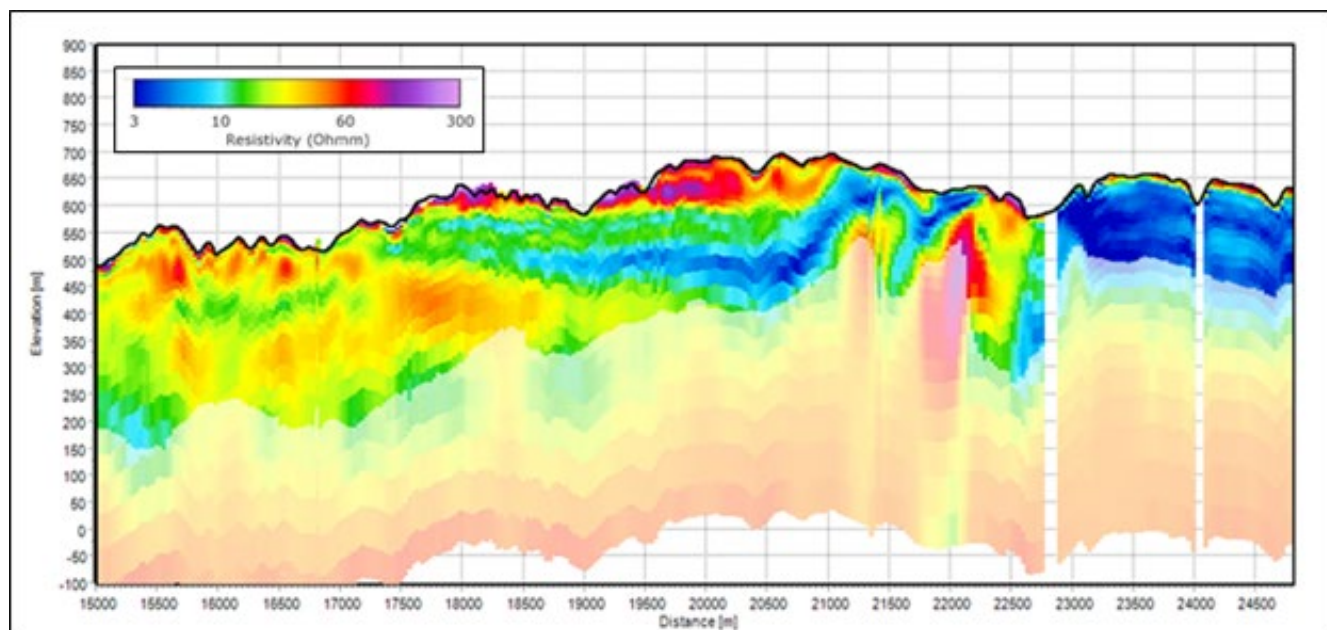
Figure 2.2. An example of the airborne electromagnetic data from the California Department of Water Resources statewide survey of the groundwater basins. Figure taken from the website https://water.ca.gov/Programs/Groundwater-Management/Data-and-Tools/AEM as an illustration of the potential depth resolution of the Central Valley lithology.

imaging the shallow subsurface.

An example of the high-resolution data is displayed in Figure 2.2. These observations could be used in conjunction with the Central Valley textural model of Faunt et al. (2010) to construct a higher resolution model that extends to the base of the lower aquifer.

While the approach by Lees et al. (2022) is useful for understanding the time scale of inelastic deformation at a particular site, it requires a substantial amount of data, information that is not typically available within the Central Valley. For example, it requires a long record of well water levels and measurements in both the upper unconfined aquifer and in the lower confined aquifer. As noted below, water level observations from wells in the Central Valley are inconsistent, with most wells sampled only twice a year and over time intervals that rarely exceed one or two decades. Furthermore, the depth sampling of lithology in wells is rarely less than 5 meters (16.4 ft) and often restricted in depth, so that researchers often lack information on the distribution of fine-grained sediments that are needed to compute the time constant τ. Airborne electromagnetics (AEM) may help in mapping the fine-grained sediments, but these observations are typically only sensitive to the first few hundred meters of sediments. Hence, more work is needed to apply the Stanford approach to the entire basin. Areas to explore are the incorporation of digitized electrical logs from existing state databases. Currently very few of these logs are in digital form and some effort needs to be extended to accomplish this. Furthermore, alternative methods, such as magnetotellurics, which are sensitive to deeper variations in electrical conductivity need to be incorporated with the AEM and well log information to construct a complete picture of the Central Valley lithology and freshwater volume.

3. Integrated Data Study.
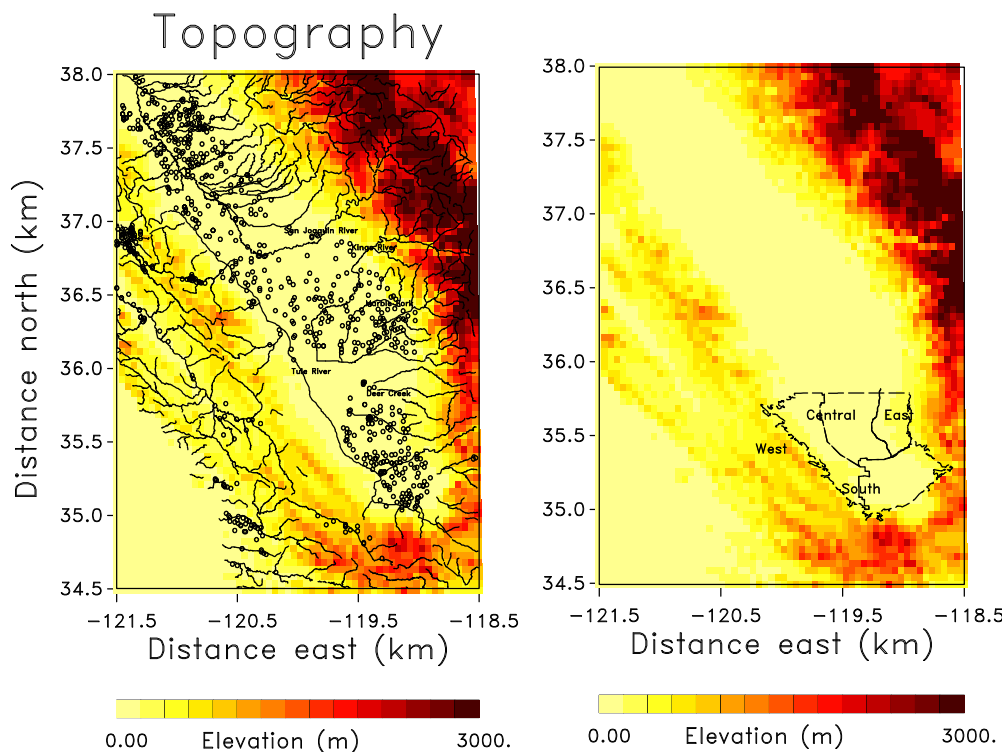
Figure 3.1. Topography of the San Joaquin Valley and the surrounding mountain ranges. (Left) The open circles denote wells with fairly extensive water table depth estimates. Major rivers and streams flowing into the valley are also indicated by the solid curves. (Right) Central Valley topography with the boundaries of the regions of the KGA plotted as solid and dashed lines.

The KCS lies at the southern edge of California's San Joaquin Valley is best understood when viewed as an integrated system. That is, even though the subbasin has unique characteristics it is influenced by large scale variations, such as regional precipitation, large-scale groundwater withdrawal adjacent to its northern boundary and other factors. Therefore, this study begins with an overview of yearly variations of the levels of the groundwater table in wells, gravitational mass changes as measured by the Gravity Recovery and Climate Experiment (GRACE) satellite data, and ground deformation as observed by the Sentinel Interferometric Synthetic Aperture Radar (InSAR) satellites operated by the European Space Agency. For the GRACE data, this initial large-scale approach is necessary because the inherent resolution is of the order of 300 km (186.4 miles) and encompasses the entire Valley. Furthermore, the Valley is an extremely large, enclosed basin (Figure 3.1). Therefore, it is difficult to define definite boundaries where one region does not influence another. In fact, data show that precipitation runoff and base flow from the adjacent Sierra Nevada impacts the large-scale gravity field within the San Joaquin Valley.

The freshwater hydrodynamics, and subsidence related to groundwater extraction, within the axis of the basin is strongly influenced by the laterally extensive Corcoran Clay, which varies by composition and in depth (Figure 3.2). The Corcoran Clay provides a barrier (aquitard) to impede groundwater flow and divides the sediments in the San Joaquin Valley into two main aquifers: a shallow unconfined aquifer that lies above the Corcoran Clay,
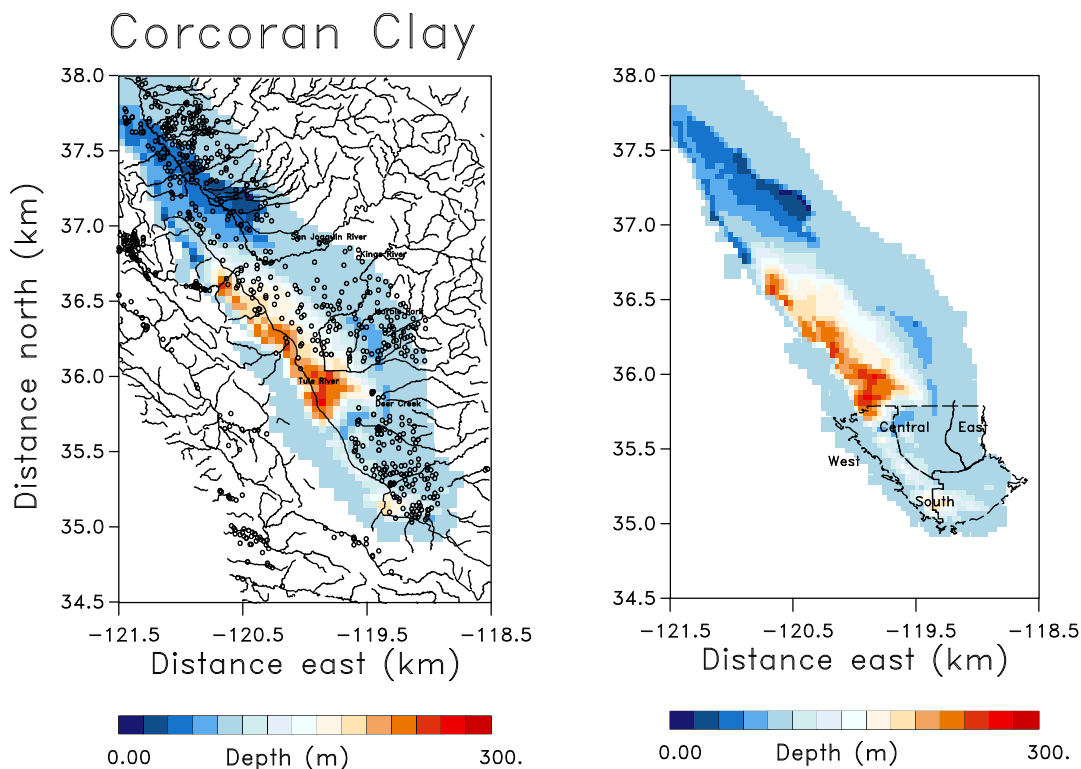
Figure 3.2. The approximate extent and depth of the Corcoran Clay (Left) Solid lines are rivers and streams, Unfilled circles are observation wells. (Right) The four sub-regions of the Kern County Sub-Basin (KCS) are plotted in this panel.

14

and a deeper confined aquifer below the Corcoran Clay. Because of the increasing number of wells that penetrate the Corcoran Clay and are open (screened) over a considerable length, the barrier is an imperfect one and there is likely communication between the two. However, the fact that the vertical permeability is generally an order of magnitude lower than the horizontal permeability helps to isolate the two aquifers. The Corcoran Clay is particularly important with respect to surface subsidence in the KCS because confined aquifers, and their associated effective stress changes typically lead to significant ground deformation. That is, because under most conditions the upper boundary of the unconfined aquifer is a constant pressure boundary (near atmospheric) and fluid is able to flow relatively freely to the surface, the effective pressure changes do not build up sufficiently to cause significant ground deformation. Note that the anisotropic permeability could allow for some confinement, but that does not appear to be a notable effect and most subsidence is found where wells penetrate the Corcoran Clay and reduce the pressure in the confined aquifer leading to dewatering of the clays. Lees et al. (2022) estimate that since 1952 roughly 80-90 percent of all compaction has occurred in the lower aquifer.

Well completions are documented based upon current permitting practices. There are over 1 million well completion reports available from the state of California databases. These well databases are useful for determining the distribution of wells within the Valley in general, and for finding regions, such as the Central
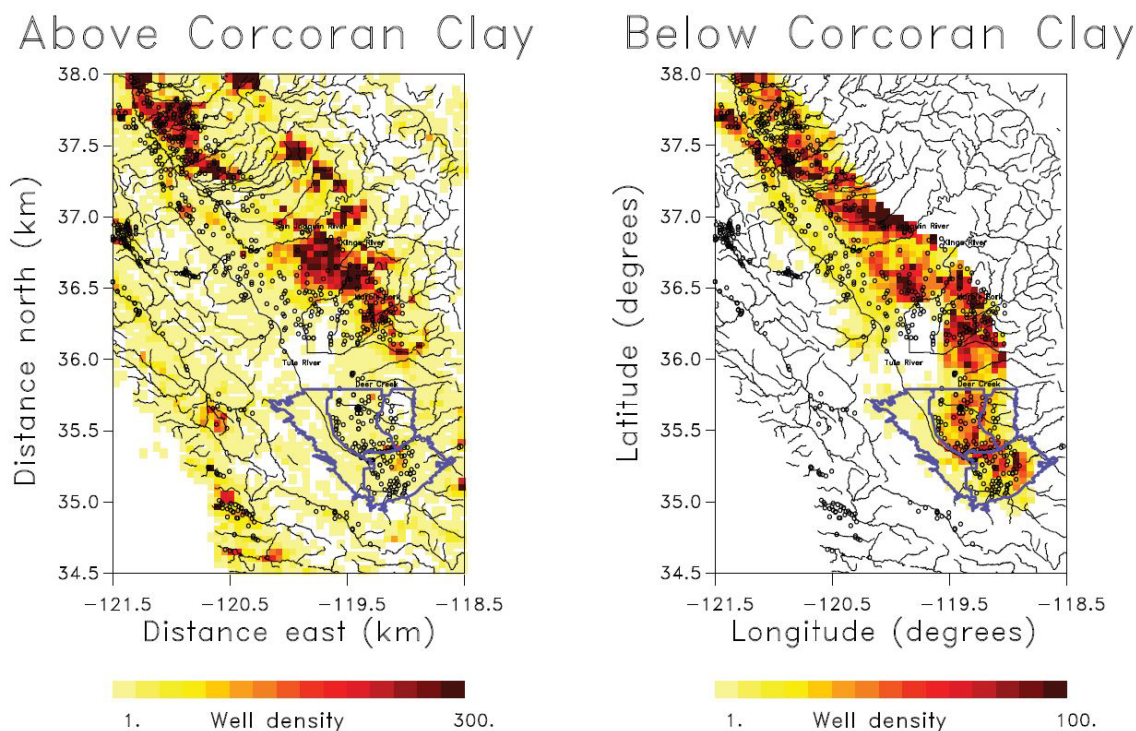
Figure 3.3. (Left panel) Density of wells that do not penetrate the Corcoran Clay. (Right panel) Density of wells penetrating below the Corcoran Clay into the lower confined aquifer.

Region of the KCS where many wells penetrate the Corcoran Clay in particular (Figure 3.3). Due to the topography of the Corcoran Clay shown in Figure 3.2, the regions where a greater density of wells penetrate into the lower aquifer are those areas where the clay aquitard is shallower. Along the western side of the KCS and
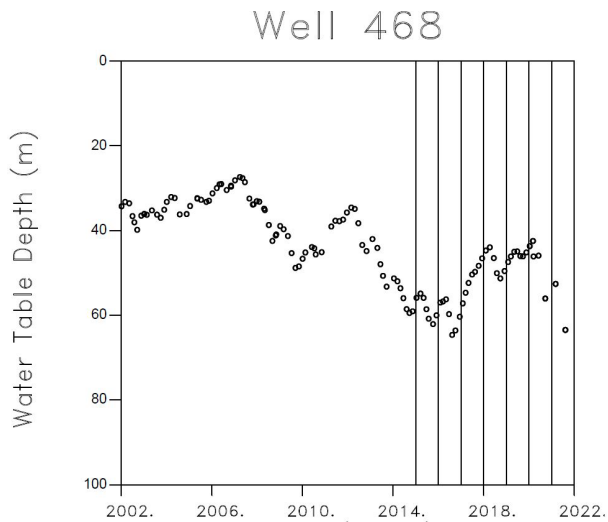

Figure 3.4. Example of a density sampled monitoring well located in the San Joaquin Valley.

the Kern fan, the Corcoran Clay or its equivalent are known to be discontinuous or even absent in places. This is shown in greater detail in Figure 3.33 where this report focuses on the well distribution in the KCS.

Water Level Measurements
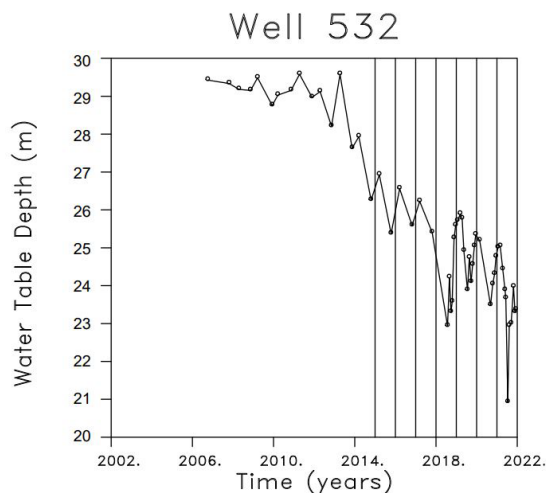
Figure 3.5. Example of typical sampling density of most monitoring wells in the San Joaquin Valley which is two observations per year. This example well is located at longitude -120.9800 and latitude 37.7985, in the upper-left corner of Figure 3.6. Note the seasonal changes in the water the table within a given year, and the long-term lowering of the water table over many years.

Another useful aspect of the groundwater of the USGS JPL well databases is the information that they provide on the location of the water table in the San Joaquin Valley. Our data set, described in Kim et al. (2020), contains wells from five well datasets, from the California Department of Water Resources and the U. S. Geological Survey.
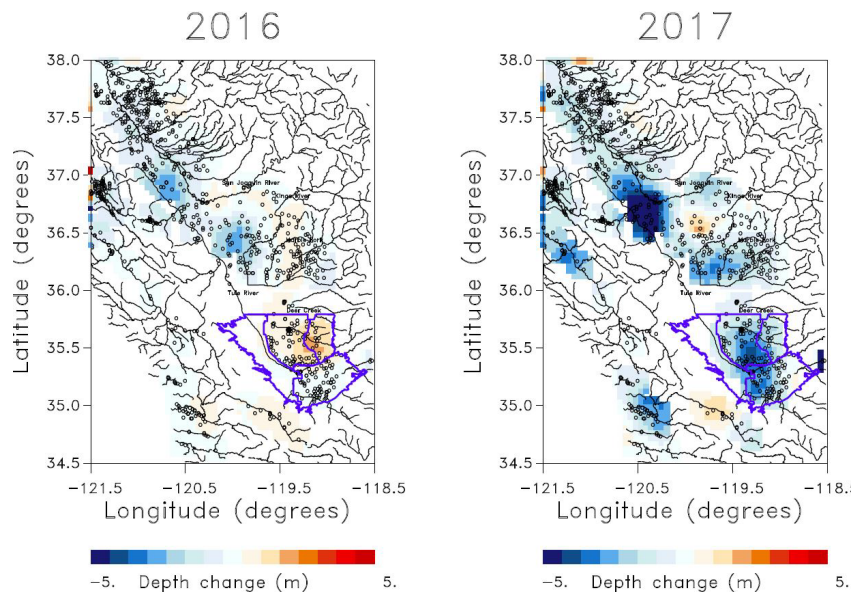
Figure 3.6. Water table depth changes, where negative values indicate upward movement of the water table. The wells that were used to estimate the depth changes are shown as open circles. The major rivers are plotted as solid curves.

Historically well monitoring in the Valley was not well-coordinated. Recently, the California Sustainable Groundwater Management Act (SGMA) has required Groundwater Sustainability Agencies (GSAs) to monitor twice yearly (Spring and Winter) to assess for chronic lowering of groundwater levels and changes in groundwater storage. Therefore, sampling density of the well shown in Figure 3.5 is much more typical of most available monitoring wells.

As in any dynamic groundwater system, there is the potential for outliers due to pumping interference between wells, equipment malfunctions, human error in recording data and other deviations. Such outliers can skew the averages of water table elevation changes. However, to minimize the influence of outliers, a large number and wide distribution of groundwater wells are utilized, and water table depth estimates are averages over all wells that were sampled at least twice yearly. In this study all wells that had jumps in water table depths of more than 15 m (~49 ft.) were removed before averaging.
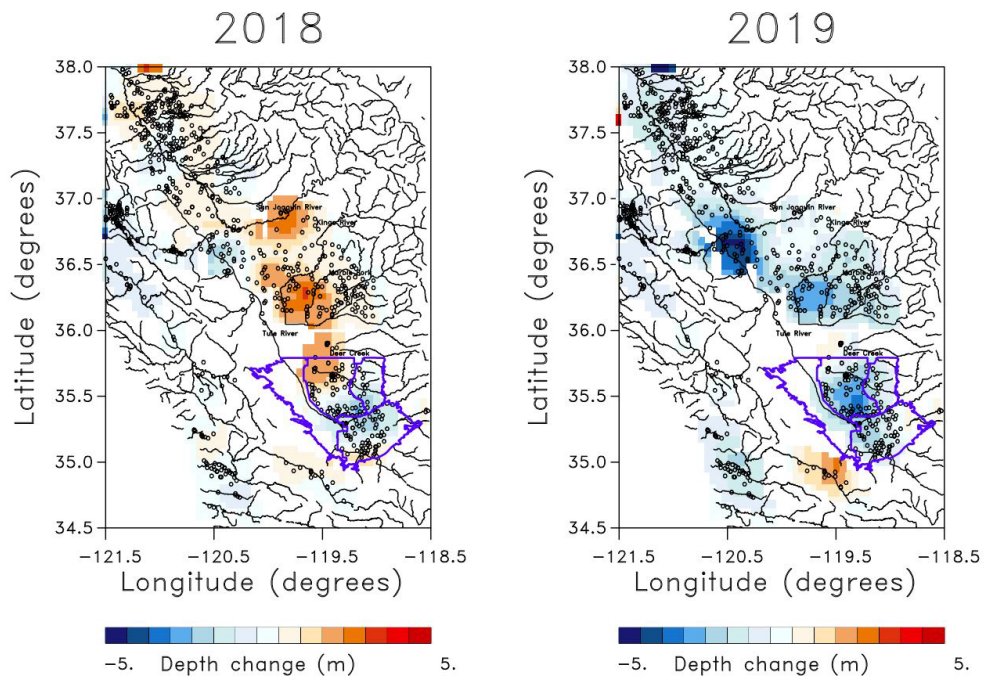
Figure 3.7. Estimated water table depth changes for water years 2018 and 2019.
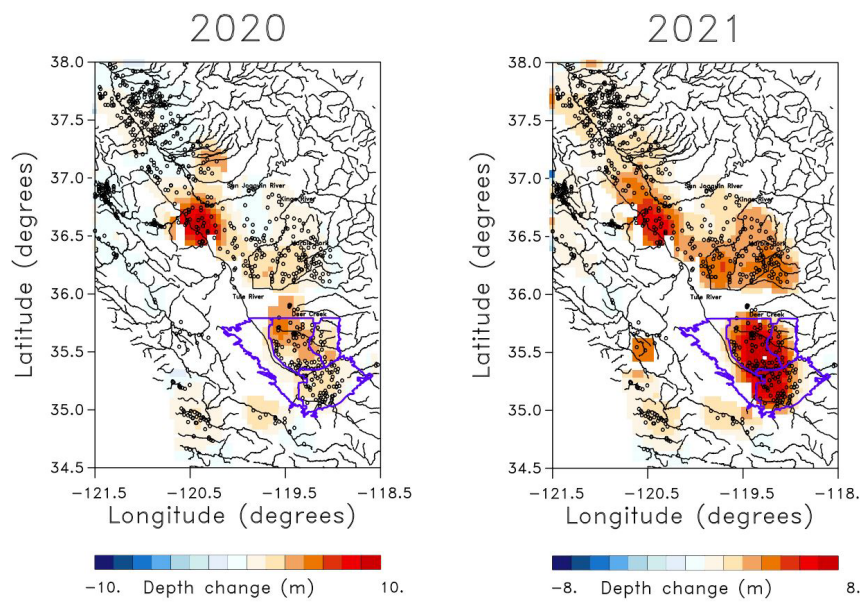

Figure 3.8. Estimated changes in the depth to the water table for the water years 2020 and 2021.

18

The estimated water table changes for water years 2016 and 2017 are shown in Figure 3.6. A negative change in depth is an upward movement of the water table. In Figure 3.6 one can observe the significant and large-scale upward movement of the water table in 2017 when there was significant precipitation due to the arrival of a number of atmospheric rivers. Similarly, in Figure 3.7, we observe water table depression in water year 2018, a year of low rainfall, and water table recovery in 2019, another water year in which numerous atmospheric rivers provided abundant precipitation. Finally, 2020 and 2021 were relatively dry years and groundwater and available import and banked surface water usage likely increased. In portions of the KCS the fluctuation of water levels between 2018 and 2019 appear to be on the order of 2 m and 4 m (6.6 ft. To 13.1 ft.). The potential rate of subsidence may have been ameliorated by the usage of import and banked surface water. As shown in Figure 3.8, the water table drops in 2020 and even more significantly in 2021. Thus, the well observations do contain coherent features and can be useful in assessing for changes in groundwater levels and, in conjunction with InSAR other geospatial data, provide a means of estimating large-scale (broad based) changes in groundwater storage. Note that the general features observed in these maps of water table depth changes are seen in the densely sampled table depth time series shown in Figure 3.4, with a significant elevation of the water table in water year 2017 and another smaller upward movement in the water year 2019.
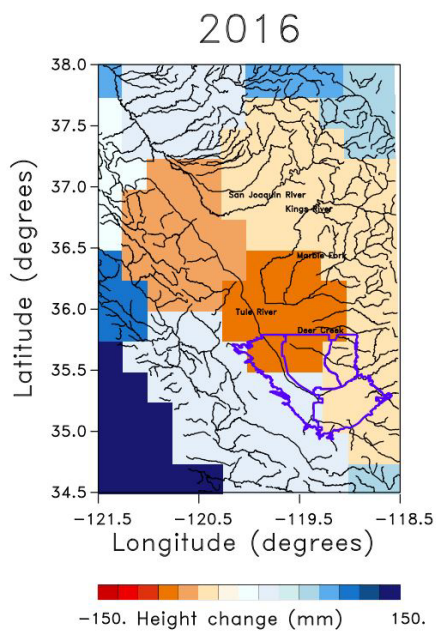
Gravity Recovery and Climate Experiment Data

Figure 3.9. Changes in the equivalent water height derived from the GRACE satellites.

Another source of observations that provide useful information on the changes in water volumes in the San Joaquin Valley and KCS is provided by large-scale gravity changes, as measured by NASA's Gravity Recovery and Climate Experiment (GRACE) satellite pair. Typically, the most significant change in mass in a basin are due to changes in water volumes in its various forms such as precipitation, underflow, soil moisture, and groundwater.

Thus, GRACE changes are expressed in terms of equivalent water volumes or change in the height change of a water level that leads to the same mass changes. There is a rough correlation between the decreases in equivalent water height in Figures 3.9 and 3.10 and the areas of subsidence visible in Figures 3.13-3.16. As discussed, a limitation of the global GRACE data set is that the spatial resolution is quite large, roughly 300 km (~186.4 miles). By contrast, aerial-based GRACE data is capable of providing much finer resolution. The difference in GRACE satellite-based spatial resolution makes any direct correlation between these GRACE observations and InSAR data difficult. Another limitation with respect to the utility of GRACE data for studying water volume changes is the transition from the original GRACE satellite system to the GRACE Follow-on (GRACE-FO) satellite system that occurred between the end of 2017 and early 2018. Thus, there is a gap in the data of roughly 1 year, impacting estimated in 2017 and 2018. Therefore, we only consider the changes in water year 2016 (Figure 3.9) and the years 2019, 2020, and 2021 (Figure 3.0). A negative value in Figure 3.10 indicates a decrease in water volume. One can see the increasingly strong water volume decreases, particularly in 2021 a year of extreme drought in the KCS and the majority of California. The distribution of volume increases and decreases can be complex, but in general there seems to be volume increases to the west and southwest and
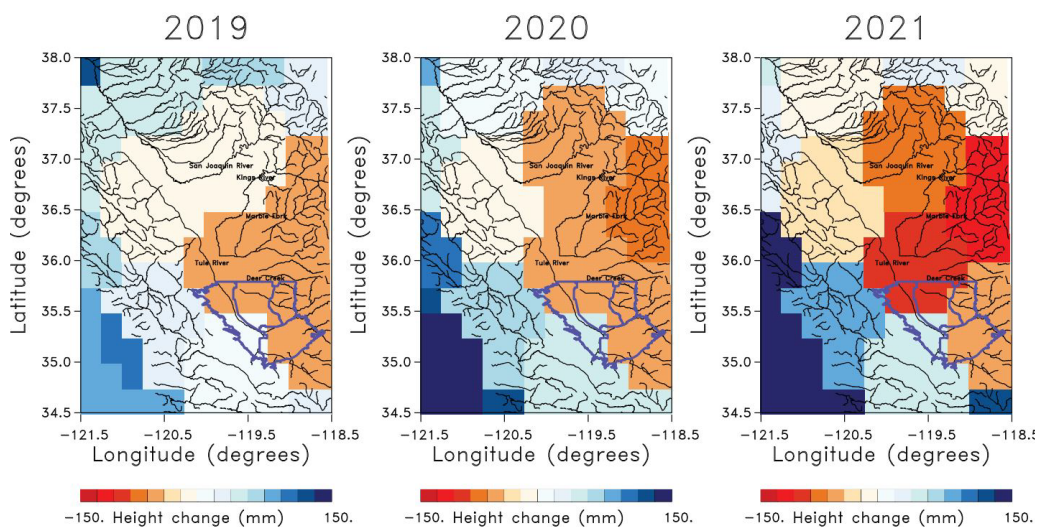

Figure 3.10. GRACE gravity changes for the water years 2019, 2020, and 2021.

volume decreases to the east. The strong eastern volume decrease may reflect the decrease in snow mass and groundwater in the Sierra Nevada to the east. As mentioned earlier, the spatial resolution is 300 km (~186.4 miles), so it is only the total volume changes in these panels that are well determined. In the KCS the GRACE data seems to indicate slight increases in water volume in much of the sub-basin, with possible decreases in water volumes in the eastern sub-area. Again, the spatial resolution of the satellite-based GRACE data is low, and the equivalent height is a large-scale measure that is likely averaging volume increases and decreases. Figure 3.11 displays the monthly changes in total water volumes for the four years that are plotted in Figures 3.9 and 3.10. For 2016 there is a slight increase in water volume at the very end of the year, and a much larger increase
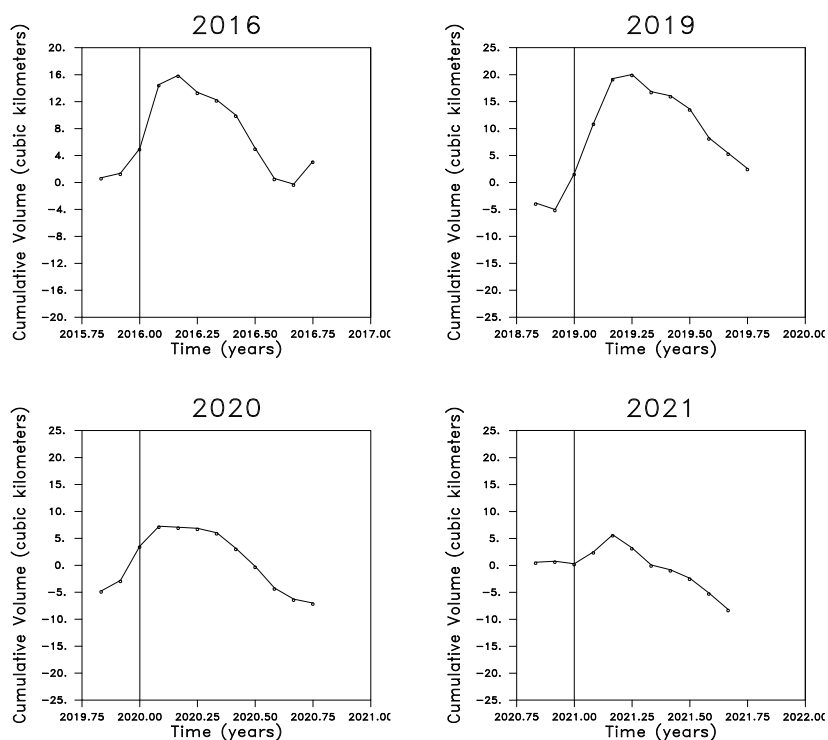
Figure 3.11. Monthly water volume changes for the four water years 2016, 2019, 2020, and 2021. The vertical line denotes the start of the calendar year.

in the wet year 2019. There is an increasing loss in water volume in the San Joaquin Valley and KCS in 2020 and 2021. These values are in line with the observed water table depth changes shown in Figures 3.6, 3.7, and 3.8. They are also compatible with the InSAR range changes that are plotted below (Figures 3.13-3.16).

Interferometric Synthetic Aperture Radar

Interferometric Synthetic Aperture Radar (InSAR) has become the geodetic method of choice for monitoring subsidence associated with fluid extraction. In fact, some of the earliest applications of InSAR were observations

related to subsidence due to geothermal production (Massonnet et al. 1997, Carnec and Fabriol 1999). The characteristics that contribute to its appeal for long-term monitoring over large areas are the fact that it is a remote sensing technique, usually satellite-based, it samples areas with high spatial resolution, and satellite revisit times are months to weeks and even days. While the technology and processing associated with estimates of surface deformation are sophisticated (Gabriel et al. 1989, Massonnet and Feigl 1998, Bürgmann and Thatcher 2013, Ferretti 2014), the underlying principle is similar to that of echo location (Figure 3.12).
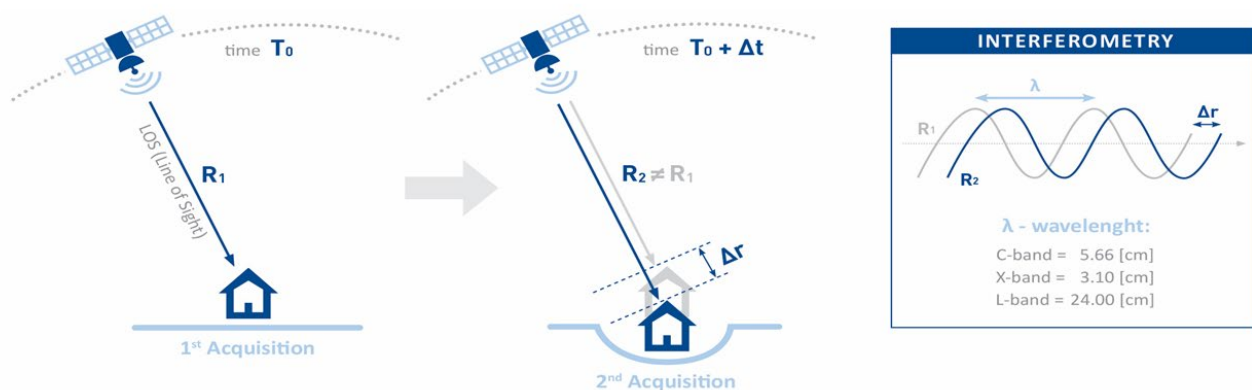
Figure 3.12. Principles underlying Interferometric Synthetic Aperture Radar (InSAR) estimates of line-of-sight (LOS) displacements. Acquisitions at different times provide time series of microwave reflections from points on the Earth. If the surface characteristics do not change substantially, the phase shifts between the time series can be related to the change in line length, the range change.

A microwave chirp from an orbiting satellite propagates to the Earth's surface where it is reflected from various scattering points and the return is stored for later use. Several stages of processing result in very accurate estimates of changes in the effective signal phase for points on the surface of the Earth (Ferretti 2014). These interferograms are then mapped into range change, the movement of the object in the line-of-sight direction (Figure 3.12). Thus, the three-dimensional displacements are projected onto the direction in which the satellite is 'looking'. As might be imagined, changes in the characteristics of the Earth's surface between satellite passes can have a pronounced effect on the estimates of range change. Extensive vegetation, snow cover, and wind-blown sand are some of the more common issues, particularly for the shorter wavelength C-band InSAR data. However, processing technology has advanced and improved satellite hardware and orbital configurations, including shortened return time of 6 days, have helped to overcome or mitigate many of these problems (Lanari et al. 2004, Hooper 2008, Ferretti et al. 2011, Samsonov and d'Oreye 2012).

InSAR deformation data is affected by a variety of natural phenomena including, but not limited to, atmospheric moisture, vegetation transpiration, and ionospheric noise. Further, small differences in deformation values

(rates) can also be realized depending on the process used for image stacking and the type of processing and smoothing algorithm utilized.

The data used in this study were gathered by the European Space Agency's Sentinel 1-2 satellite C-band system, using data from 216 orbits, spanning a time interval from early 2015 until late in 2021. The time interval between satellite passes varied during this time period, starting at 12-day orbits during the first few years and transitioning to shorter 6 day returns after a reconfiguration in 2018. The shorter orbital intervals improved the accuracy of the estimates and mitigated the effects of vegetation changes due to agriculture, improving spatial coherence.
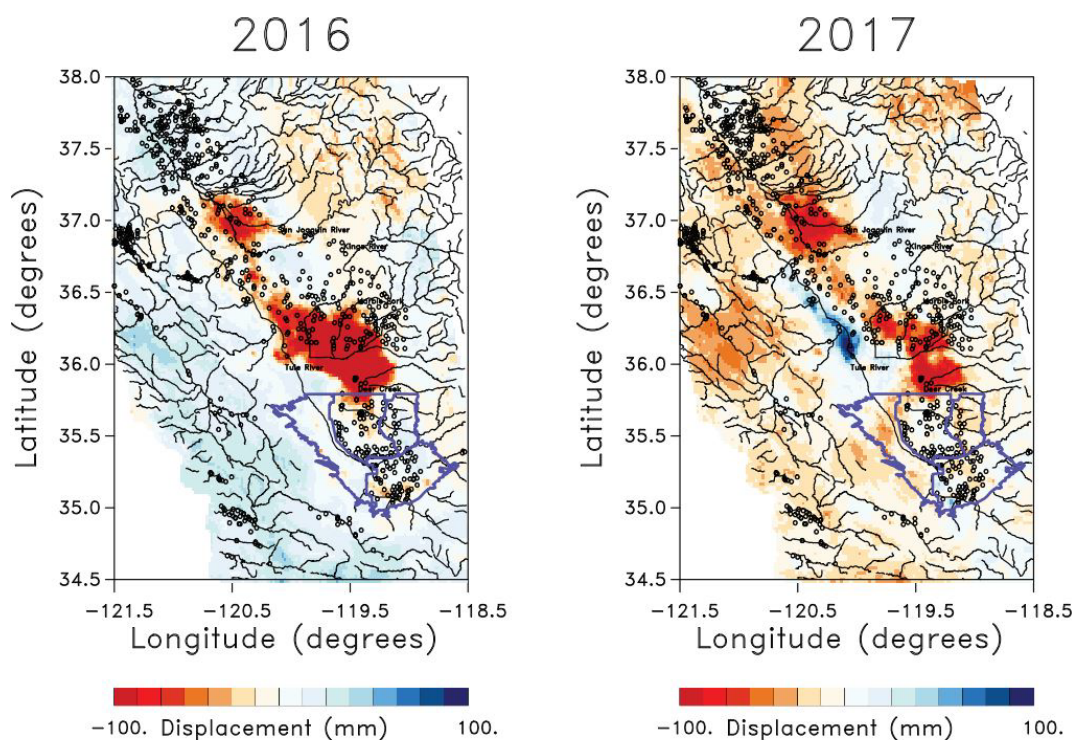
Figure 3.13. Line-of-sight (LOS) displacements for the water years 2016 and 2017. The open circles denote wells with useful water level observations that were used to compute the changes shown in Figures 3.6, 3.7, and 3.8.

The estimated accuracy of the 2015-2017 Sentinel InSAR estimates, obtained by comparison with continuous GPS data, was found to be 18 mm or 0.70 inches (Towill 2021). For this study we considered the line-of-sight displacements that occurred during the six water years 2016, 2017, 2018, 2019, 2020, and 2021. These intervals capture the variations between the wet years in 2017 and 2019 and the other years when there was less precipitation. In Figure 3.13 we plot the LOS displacements for water years 2016 and 2017.

A recent (2021) InSAR study conducted by Earth Consultants International (ECI) on behalf of the KCS processed 172 Sentinal-1 radar images to produce 86 paired synthetic aperture radar images which were combined to produce 526 interferograms spanning the period 2015 to 2020. The data were processed multiple times to reduce atmospheric effects and improve accuracy. As a final check the data were ground-truthed against 13

continuous geospatial position data. The ECI study data has a vertical resolution of approximately 0.094 inch/year (2.4mm) and a horizontal pixel resolution of around 82ft. (25 meters), with no space between pixels. A key finding of the 2021 ECI report was that Previous JPL/NASA studies may have overestimated subsidence rates associated with seasonal groundwater pumping (i.e., agricultural use). ECI suggests this phenomenon may be the result of the short time intervals (i.e., often less than five years) related to the InSAR acquisition in those studies. These discrepancies were recently corrected.

The large-scale and long-term subsidence bowls north of the KCS due to groundwater withdrawal is clear for both 2016 and 2017. However, in the water year 2017 we observe overall upward line-of-sight displacement (i.e., recovery) near the center of the panel, signifying rebound due to the increase in effective pressure in the confined aquifer. This is an elastic effect that is distinct from the inelastic permanent loss of aquifer/aquitard volume that is associated the lowering of fluid pressures during years when groundwater withdrawals are significant. For the KCS, which comprises the southern-most parts of the panels in Figure 3.13, the pattern is somewhat more complicated. The center of the subsidence bowl lies to the north of the KCS and the deformation associated with it is only significant at the northern edge of the KCS. Subsidence associated with the Lost Hills and Belridge oil fields are visible in both the 2016 and 2017 panels. These are discussed in more detail below.
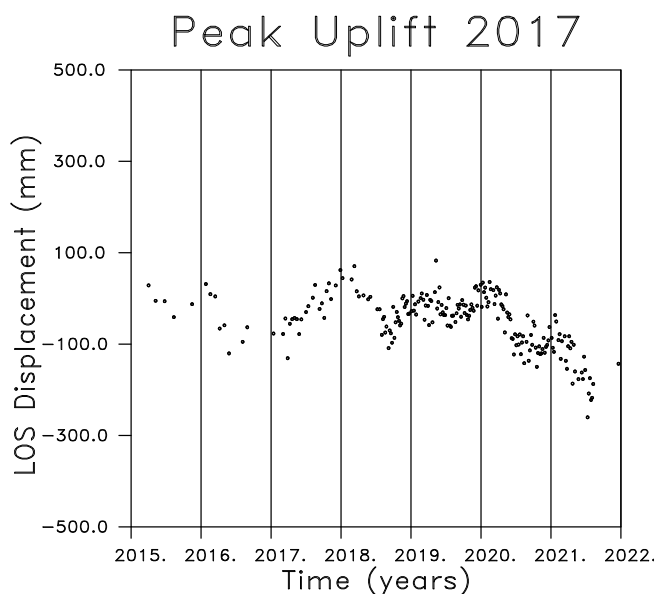

Figure 3.14. Line-of-sight (LOS) displacements between 2015 and 2022 derived from the Sentinel 1A/B SAR observations.

The change from yearly subsidence to uplift in 2017 is evident in Figure 3.14 where we plot the line-of-sight displacements for the point with the peak yearly uplift in water year 2017 [see Figure 3.13]. The change in satellite return times from 11 to 6 days is evident in this figure. There is a clear upward trend from October 2016

24

to October 2017. Furthermore, the increasing subsidence in drought years 2020 and 2021 is clear in Figure 3.14. Thus, the elastic rebound during the wet year 2017 is based upon solid evidence and supports the monthly elastic changes described in Vasco et al. (2022). After removing the long-term subsidence, they found residual uplift,
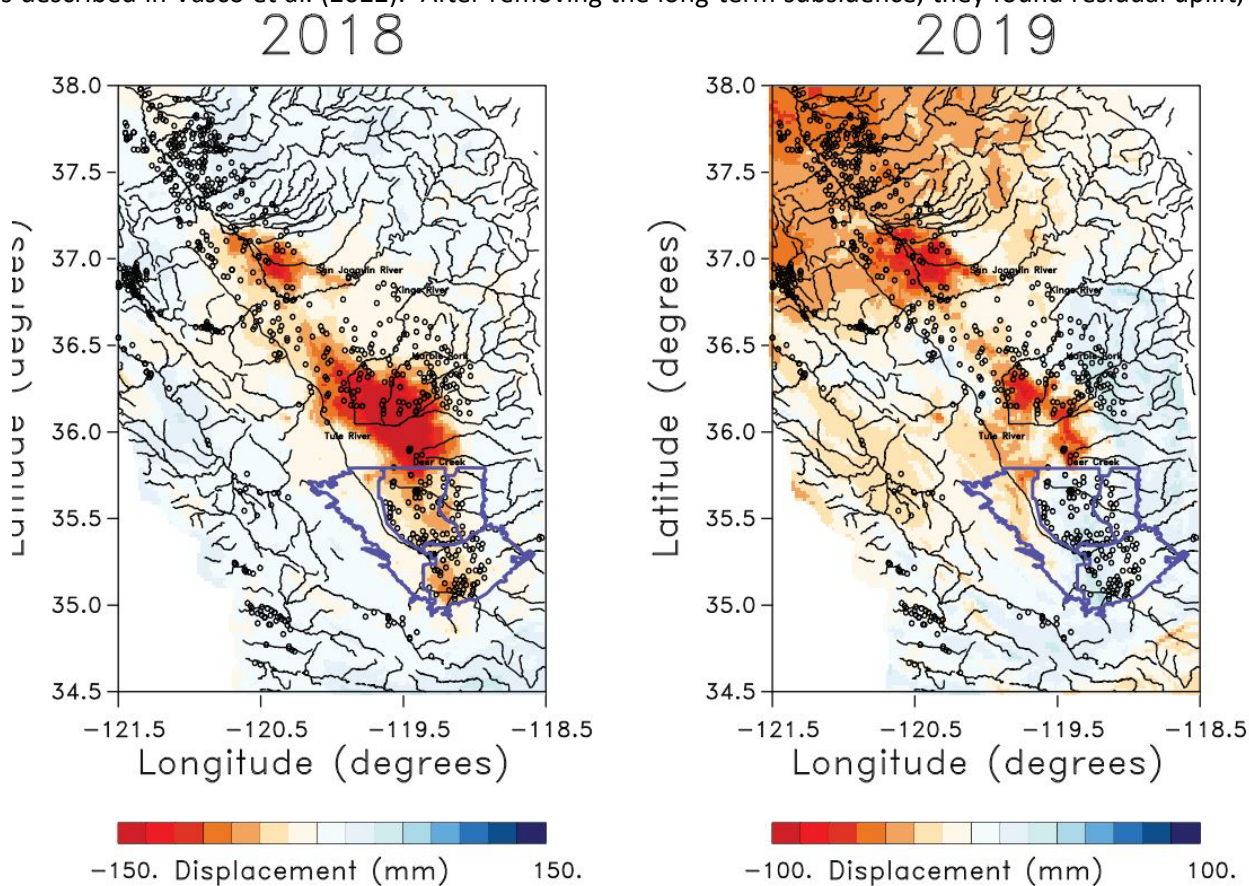

Figure 3.15. Line-of-sight displacement for water years 2018 and 2019.

thought to be due to recharge in the wet years 2017 and 2019. A general pattern of uplift is initiated on the margins of the KCS in the late winter and spring. Over time the uplift "migrated" to the north and west along the axis of the valley. In the particularly wet year of 2017 the migration of uplift continued through July, August, and September, associated with base flow from surrounding highlands and the use of imported water and banked surface water. Such hydrodynamics are similar to regional flow patterns found earlier by Neely et al. (2021). In particular, they noted the rebound along a portion of the valley axis, as seen in the left panel of Figure 3.13. As can be seen in the time series in Figure 3.14, starting in 2018 the Sentinel-1 InSAR temporal sampling increased to an observation every 6 days, which allow for temporal averaging and improved estimates of line-of-sight displacements. This improved sampling also helps to better refine the relative contributions of oil field and   agriculture   fluid   volume   changes   to   the   subsidence.
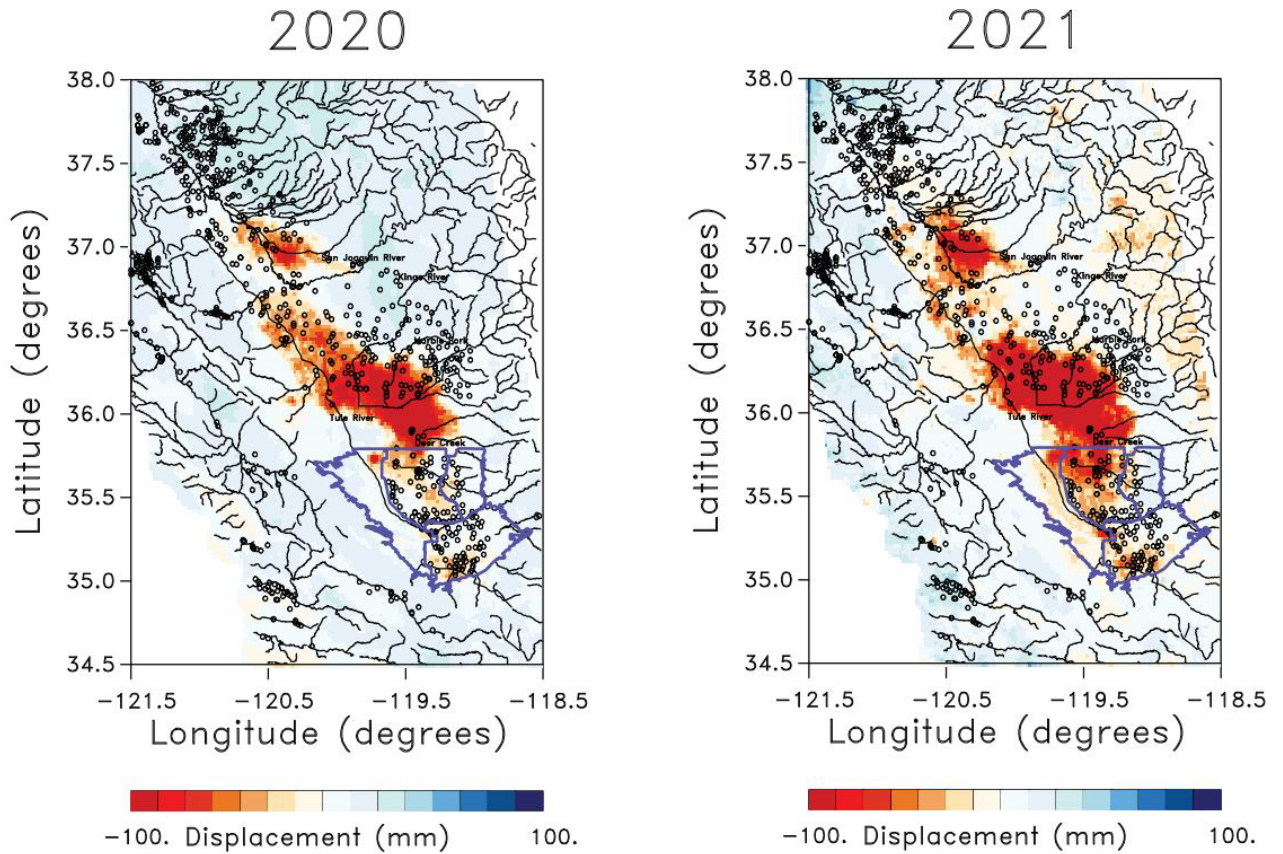
Figure 3.16. Line-of-sight displacement for water years 2020 and 2021.

The next two water years, 2018 and 2019 are displayed in Figure 3.15. The subsidence in the water year 2018, which had low to normal rainfall is similar to that seen in 2016 (Figure 3.13), with wide-spread depression of the Central Region of the San Joaquin Valley north of the KCS. In the KCS we observe overall subsidence as well though the magnitudes are much smaller than the peaks seen in the subsidence bowls to the north. In the wetter year of 2019 the areas of peak subsidence are more concentrated, and the ground surface is slightly elevated in the Central Region that experienced significant uplift in 2017 (Figure 3.13). There is generally uplift in the KCS, though the areas around the Lost Hills and Belridge oilfields display concentrated areas of subsidence that are likely due to non-SGMA-related activities. The larger scale and smaller changes in the region surrounding the basin are complicated and may reflect the effects of both subsidence due to elastic loading and unloading from the shallow aquifer, as well as subsidence due to inelastic compaction. In the two water years 2020 and 2021 the San Joaquin Valley and the surrounding region experienced little rainfall and water deliveries to farms and ranches in the area were reduced substantially from normal deliveries. Therefore, groundwater usage climbed inducing further subsidence. The rate and magnitude of subsidence may have been ameliorated to some extent by the use of imported water and banked surface water. The InSAR-derived line-of-sight (LOS) displacements for these years are shown in Figure 3.16. There is overall subsidence in the central portion of the

KCS, but the pattern is complicated, particularly in 2020. Interestingly, the subsidence above the oil fields is less pronounced in 2020 but subsidence above the fields is evident again in 2021. The displacements within the KCS are discussed in more detail below.

The area of significant subsidence has broadened in 2021 and encompasses much of the San Joaquin Valley including the KCS with displacements that exceed 10 centimeters in places. The general trend observed in these yearly changes is reflected in the time series in Figure 3.14, where we see overall subsidence over time, pauses in water the years 2017 and 2019, and subsidence with increasing amplitude in the water years 2020 and 2021.

We can estimate a lower bound on the yearly aquifer volume losses in the San Joaquin Valley by examining the integrated subsidence for each interval and converting it to a volume change. Specifically, we sub-divide the region into a dense grid of pixels and examine the subsidence in each pixel. Multiplying it by the area of the pixel we can compute a volume change due to the surface deformation. Due to elasticity, the actual source volume change could be larger, so the estimate is a lower bound on the changes at depth. Also, the water volume changes in the unconfined aquifer do not necessarily produce surface deformation, so the total water volume changes can be still larger. However, it is a useful lower bound and provides a simple measure of the volumes involved and their variation over time. In Figure 3.17 we plot the total volume changes for the water years from 2016 until 2021. The rate of surface subsidence volume change in the San Joaquin Valley at large varies between 0.4 and 1.8 cubic km per year for this interval. There is a net increase of 0.2 cubic km/year (162,143 acre-
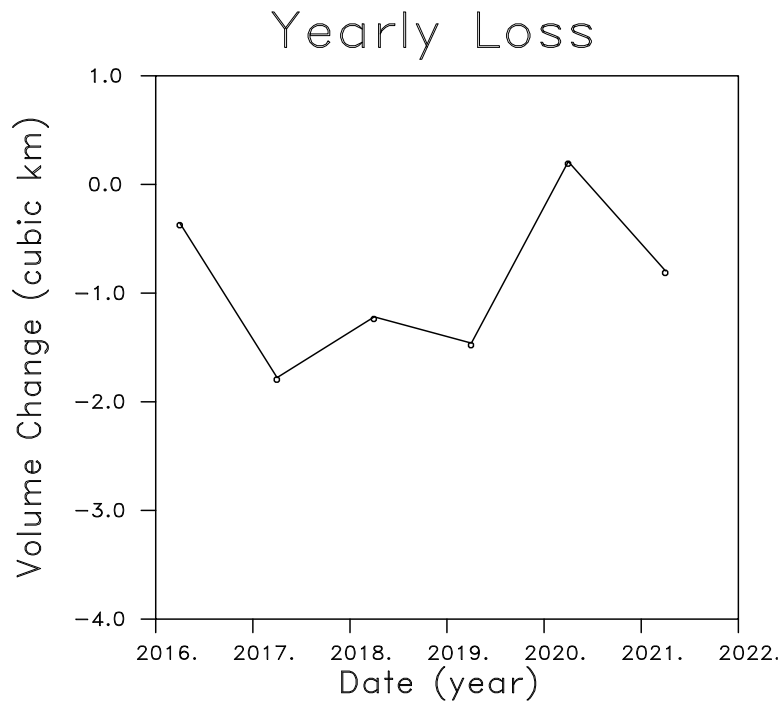
Figure 3.17. Total integrated volume changes due to surface deformation for the water years from 2016 until 2021.

feet/year) in aquifer volume from 2019 to 2020. These rates bound the groundwater depletion rates determined by Liu et al. (2022) for the total water volume loss per year which is changing over time but was 1.86 cubic km/year (1.45 million acre-feet/year) for the interval 1961-2021, 2.41 cubic km/year for 2003-2021, and possibly as much as 8.58 cubic km/year (6.9 million acre-feet/year) for 2019-2021. The rates in Figure 3.17 also agree with the rate of loss of 1.5 cubic km/year (1.2 million acre-feet/year) in Argus et al. (2022) for the southern one-third of the Central Valley that includes the KCS between 2006 and 2021. Note that the fluctuations in the rate agree with the wet years in 2017 and 2019, for these years the rate of loss decreases, and is volume increases from 2019 to 2020. There seems to be a one-year lag between the level of precipitation and the rate of loss, likely due to the time needed for the pressure loss to diffuse into the clay layers, leading to inelastic compaction. This effect was modeled by Helm (1975, 1976) and the model was recently revisited by Lees et al. (2022). As emphasized by these authors, the time constants for this diffusion depend upon the layer thicknesses and the subsidence due to effective pressure decreases can last for decades or even centuries.

In order to further our understanding of the factors influencing surface subsidence in the KCS, we followed the approach of Vasco et al. (2019) and used the InSAR line-of-sight (LOS) displacements to infer the aquifer volume changes giving rise to the observed deformation at the Earth's surface. As in that work, we incorporate the notion that fluid withdrawal from wells is the primary source of long term, yearly and longer, deformation. It should be noted that on the west side of the KCS where groundwater pumping for agriculture is scarce, the

primary source of pumping is from non-SGMA activities. To this end, we include a "penalty term" in our inversion algorithm that introduces a preference for models that have volume changes in grid blocks that are intersected by a high density of wells. Thus, we will make use of the densities of wells above and below the Corcoran Clay, as plotted in Figure 3.3. While the details of the approach are given in Vasco et al. (2019), the general approach is based upon the notion that the volume changes in the aquifer, which can be inelastic and non-linear, lead to deformation in the surrounding medium, which after some distance, lead to displacements that are small enough to be treated as elastic deformation. Thus, for a given time increment, say due to one hour or a day of pumping, the resulting aquifer deformation produces corresponding displacement within the surrounding medium and at the Earth's surface. Over time, these incremental displacements accumulated into the substantial yearly deformation that we observe in Figures 3.13, 3.15, and 3.16. The incremental deformation is assumed to generate elastic deformation outside of the grid block of reservoir volume represented in the source model.

The model developed in this study is a combination of those presented in Vasco et al. (2019) and Vasco et al. (2022). Specifically, we consider a two-aquifer model as in Vasco et al. (2022), with an unconfined upper aquifer above the Corcoran Clay, where it exists, and a confined lower aquifer below the Corcoran Clay. In areas where the laterally extensive Corcoran Clay is not found, we only allow for the upper aquifer, extended to a nominal depth of 100m (328 feet). This approach must be modified in regions where there is active oil extraction, such as in the KCS, and the volume changes should be restricted to the oil reservoir volume.

As in Vasco et al. (2019), for areas containing the Corcoran clay we introduce a penalty function for volume changes in the two aquifers based upon the well distributions in Figure 3.3. That is, we incorporate a penalty term that measures the distance from the grid block of interest to the nearest grid block containing a sufficient density of wells. The penalty is the square of this distance. Thus, grid blocks that are far from any sufficient number of wells in a given aquifer have a greater distance penalty and are only allowed volume change if it is necessary to satisfy the InSAR data. One difference in the current formulation and that of Vasco et al (2019) is that we no longer base the penalty on the strict depth of the well but rather on the depth of the well with respect to the location of the Corcoran Clay. Thus, the well distributions look somewhat different than those in Vasco et al. (2019), with few wells extending below the Corcoran Clay where it is deepest and many wells extending below it where it is shallow. Thus, the area of rebound in 2017, that is evident in Figure 3.13 does not actually contain many wells extending below the Corcoran Clay, even though it is an area with many deep wells, as shown in Vasco et al. (2019). Basing the penalty on the penetration of the wells into the aquifer below the Corcoran Clay makes sense because it is a confined aquifer and fluid withdrawn from this aquifer is much more likely to generate notable surface deformation. One notable difference between this study and that of Vasco et al. (2022) is that we are considering the total deformation for each water year, and we do not remove the long-term trend.

Thus, the subsidence, and hence the yearly volume decreases that we estimate, reflect not just the water volume changes for the given year, but also display the effects of water volume changes from years past. Still, the volume changes may provide some insight into the factors controlling surface subsidence.

We will consider the yearly changes from 2016 to 2021, starting with the estimated volume changes for 2016 that are plotted in Figure 3.18.
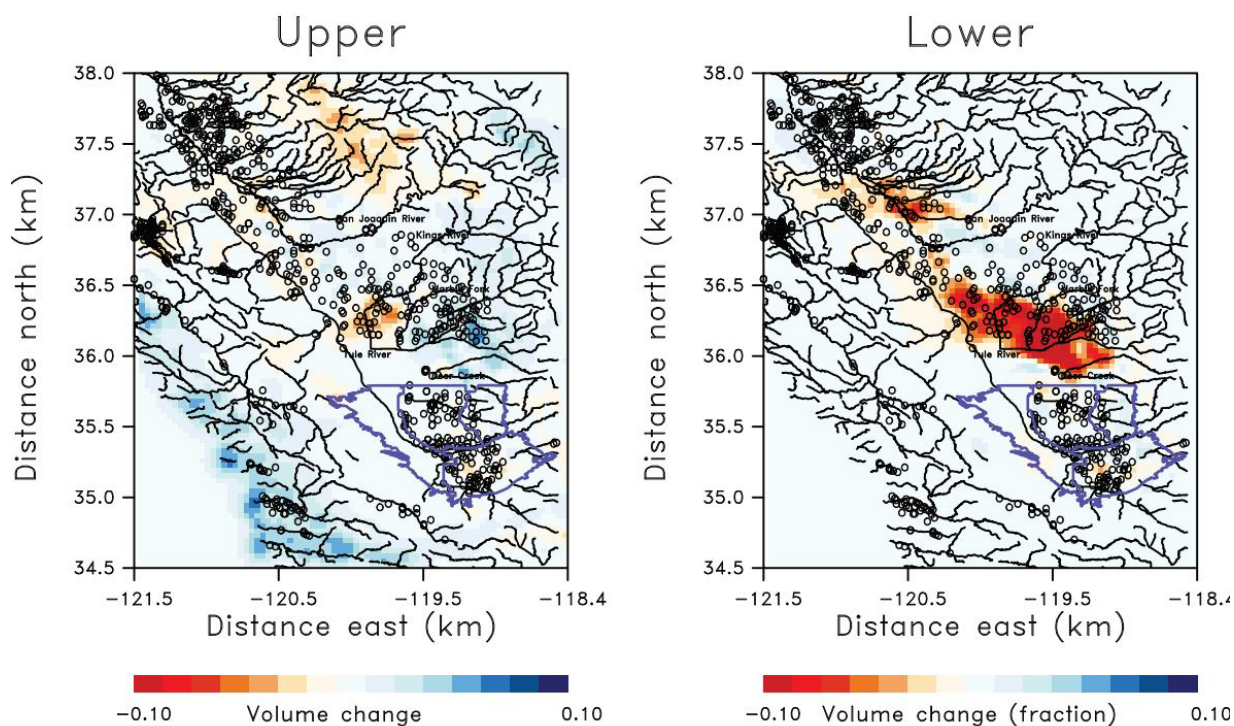

Figure 3.18. Volume changes estimated for the water year 2016. (Left panel) Fractional volume changes in the upper aquifer that lies above the Corcoran Clay. (Right panel) Fractional volume changes in the confined aquifer lying below the Corcoran Clay.

The estimated fractional volume changes for the water year 2016 are dominated by volume decreases in the confined aquifer, primarily in areas with high densities of wells penetrating the Corcoran Clay, such as areas to the north of the KCS (see Figure 3.3). This suggests that the penalty term is successful in both fitting the data and satisfying the constraint that volume changes occur where there are dense concentrations of wells. The largest area of volume decrease in the lower aquifer does extend slightly to the west of the dense configuration of wells, perhaps due to a general decrease in effective pressure in the region surrounding the wells or indicating the importance of a few deep wells in producing substantial compaction due to the weight of the overlying sediments. The inclusion of the well distance penalty does not degrade the final fit to observations significantly and the data are relatively well fit, as shown in Figure 3.19.
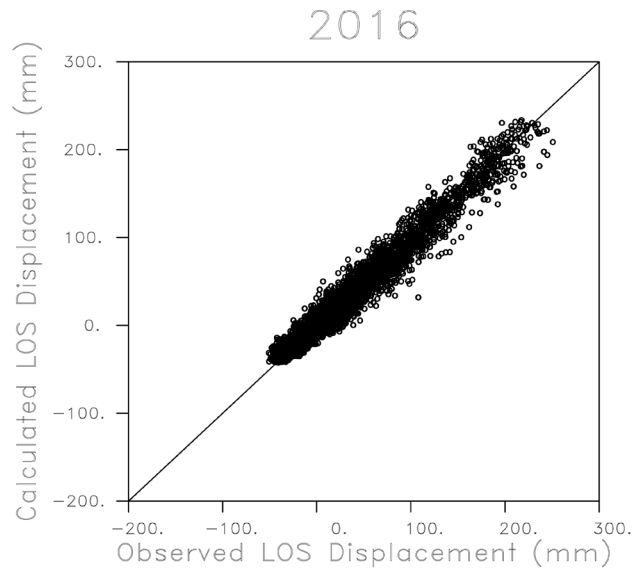
Figure 3.19. Observed versus calculated line-of-sight (LOS) displacement for the San Joaquin Valley InSAR data. The model shown in Figure 3.18 has been used to calculate the displacements.

The following water year 2017 was considered a wet year in which precipitation was higher than historical averages and this led to areas in the KCS rebounding and net uplift along the valley axis, as shown in Figure 3.13. This uplift was noted by Neely et al. (2021) and Vasco et al. (2022). An inversion for volume changes in the upper and lower aquifers during the water year 2017 displays general volume increases in the upper aquifer and volume
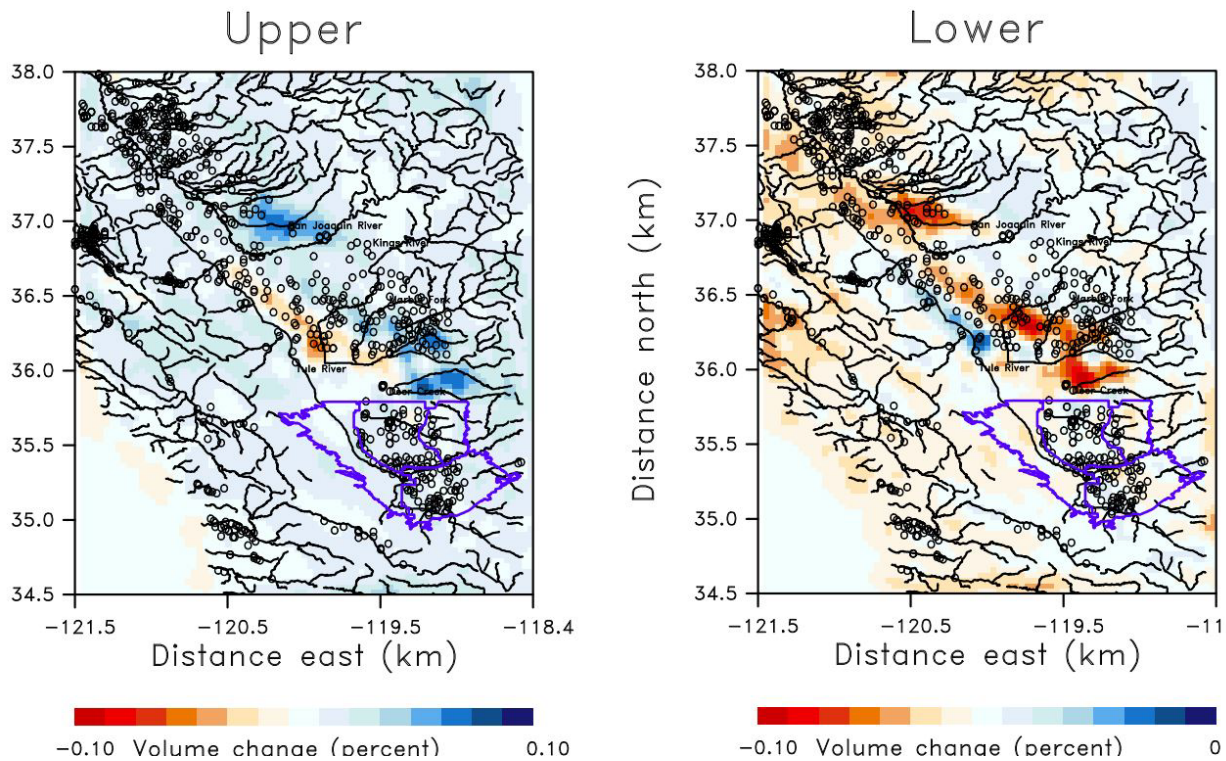
Figure 3.20. Inversion results for water year 2017. Volume changes in the unconfined (Upper) and confined (Lower) aquifers that lie above and below the Corcoran Clay, respectively.

decreases in the lower aquifer below the Corcoran Clay (Figure 3.20). The volume decreases in the lower aquifer correlate with the locations of well clusters the penetrate the Corcoran Clay, a result of the well distance penalty. However, there are volume increases in the lower aquifer in an area with few wells extending below the Clay aquitard, volume changes that are required by the InSAR LOS displacements. Note that the positive and negative volume changes in the two aquifers are not co-located in space but are slightly offset from each other. As indicated in Figure 3.21, we are able to fit the observations with volume changes that, for the-most-part, lie near well locations. The volume increase in the confined aquifer, evident as positive volume change in Figure 3.20 is
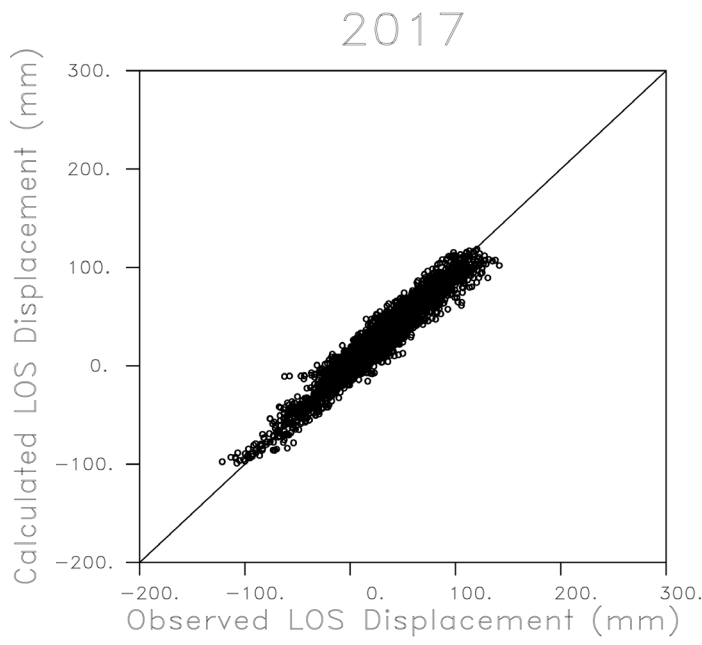
Figure 3.21. Calculated line-of-sight (LOS) displacement plotted against the observed values for water year 2017.

significant because it indicates elastic rebound in the deepest part of the confined aquifer [see Figure 3.2]. This behavior supports the observations by Neely et al. (2021) and Vasco et al. (2022) that water entering the San Joaquin Valley from the south and east makes its way to the deep central axis of the trough, increases the effective pressure within the aquifer, leading to uplift in a concentrated region. Such isolated uplift can be difficult to observe with distributed sensors, such as surface and Global Positioning System (GPS) instruments, but it is discernable via InSAR.

Global Positioning System Data

In addition to InSAR, there are also observations from the satellite-based Global Positioning System (GPS), that record time-encoded signals that are used to triangulate positions of receivers (Dixon 1991, Hofmann-Wellenhof et al. 2007, Bock and Melgar 2016). Arrays of permanent stations provide observations of three-dimensional displacements in many regions of the Valley. In the Valley itself there are over 200 high quality time series of surface deformation with observations available on a daily basis (Figure 3.22). In the KCS there are approximately
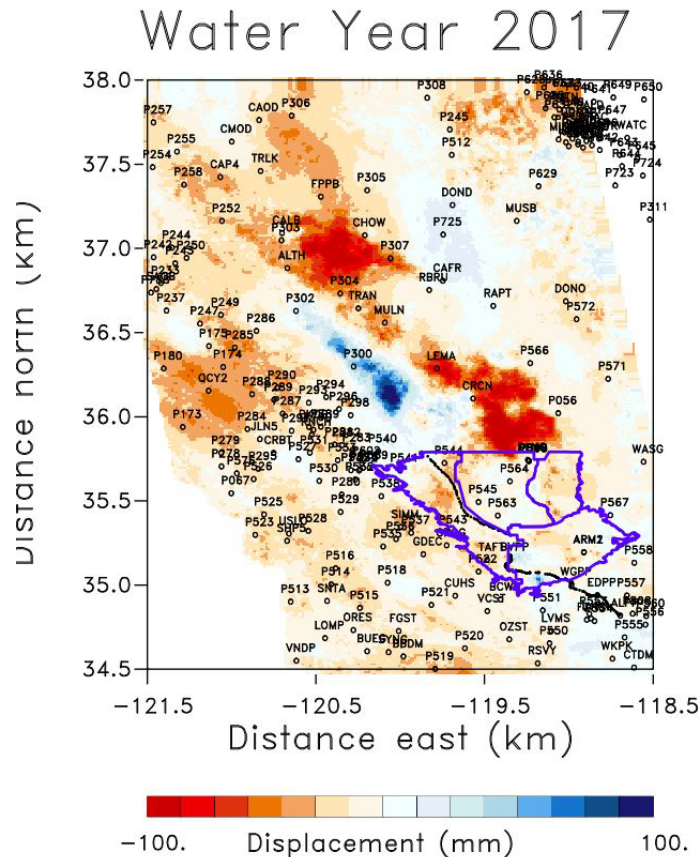
Figure 3.22. Distribution of Global Positioning System stations in the San Joaquin Valley. The locations of the stations are denoted by the open circles and the four-character name. The station locations are plotted on top of the InSAR line-of-sight displacements during the water year 2017. The curves in the southeast corner are points on the California Aqueduct.

40 GPS stations as discussed below. The basin would benefit from additional GPS stations, and the Kern Groundwater Authority has discussed this need with CASP and the DWR. This plot highlights one of the issues with such point measurements, there are important regions that are simply not sampled sufficiently by existing GPS stations. For example, the area of maximum rebound seen in the InSAR LOS displacement in 2017 is not sampled by any GPS stations. Neither are there GPS stations in the regions of maximum subsidence in the water
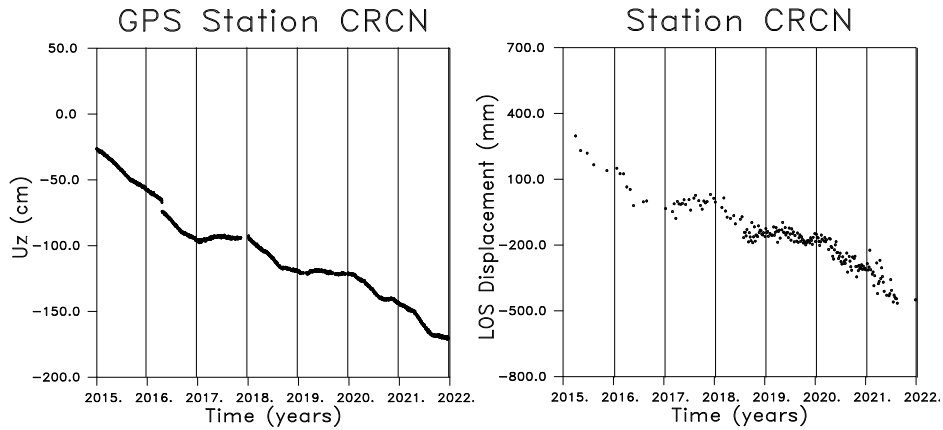
Figure 3.23. (Left) Vertical displacement recorded at the GPS station CRCN. The location of CRCN is near the town of Corcoran the area of subsidence north of the KCS in Figure 3.26. (Right) InSAR line-of-sight (LOS) displacement from the location of the station CRCN.

year 2017. Thus, while GPS stations provide exceptional temporal sampling, they can often miss crucial features that help to understand the hydrodynamics of the KCS. Thus, it makes sense to combine both InSAR and GPS observations to take advantage of the strengths of each data set. As a comparison, consider the GPS and InSAR LOS displacement at the location of the GPS station CRCN (Figure 3.23). In both data sets we observe a long-term trend of subsidence of the order of a meter (3.2 ft) between 2015 and 2022. The GPS observations are sampled on a daily basis while the InSAR observations are initial spaced 12 days apart and in 2018 the temporal spacing is reduced to 6 days. There is more scatter in the InSAR LOS measurements which do not have the
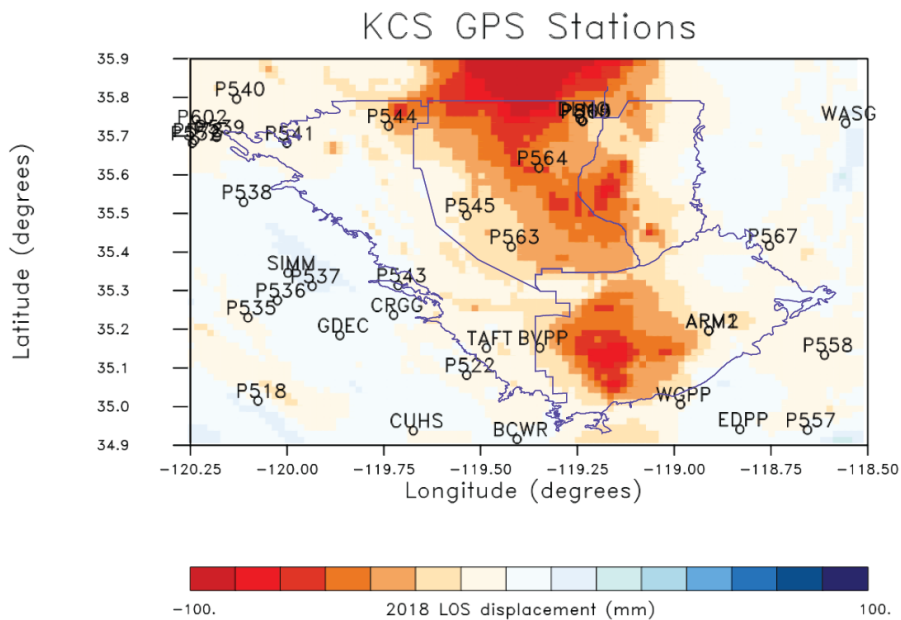
Figure 3.24. Distribution of publicly available GPS stations in the KCS.
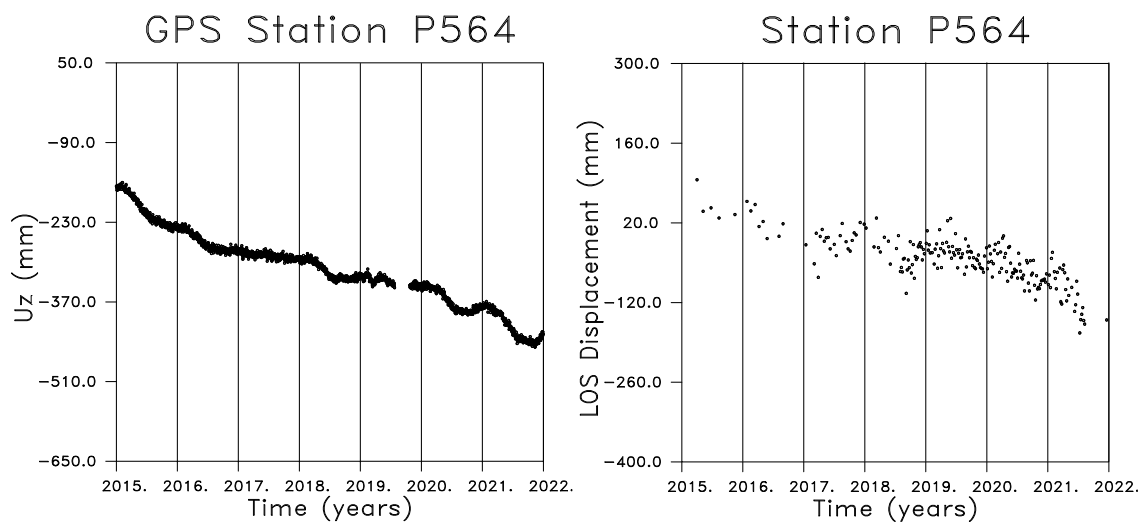
Figure 3.25. (Left) Vertical displacement observed at GPS station P564. (Right) Line-of-sight displacement derived from InSAR observations at the location of GPS station P564. See Figure 3.24 for the location of this station.

redundancy of multiple satellites that GPS observations do, requiring additional processing to remove effects such as atmospheric noise. Still, the general flattening of subsidence in 2017 and 2019 due to increased use of imported and banked surface water is visible in both sets of observations and the rate of subsidence is similar. The distribution of publicly available GPS stations in the KCS is shown in Figure 3.24.

Station CRCN is in the area of maximum subsidence north of the KCS, more typical are the rates of ground deformation seen at GPS station P564 (Figure 3.25), which lies to the south of the subsidence bowl in the KCS (Figure 3.24). Subsidence of the order of 0.3 meters (~11 inches) is observed following a largely linear trend with seasonal variations. Again, there is more scatter in the InSAR displacements, indicating a larger overall uncertainty for these observations, unless the effects can be corrected by additional processing.

Estimating Displacements in the Kern County Sub-Basin

Subsidence related to groundwater extraction can damage critical infrastructure. Regional critical infrastructure in the KCS includes the Aqueduct and the Friant-Kern Canal (Canal). Both of these structures are important to the conveyance and distribution of surface water in the KCS. Thus, pursuant to SGMA, there is a need to monitor and address such subsidence. Some key unknowns are the non-SGMA factors and climate change. Another factor noted above is the density of wells extending below the Corcoran Clay into the lower confined aquifer. Based upon Helm's model (1975, 1976), clays and clay-bearing sediments, which undergo reduction in effective pressure, are subject to inelastic compaction. Yet another factor is soils and geotechnical factors are present and influence subsidence caused by non-SGMA-related activities, particularly on the west side of the Valley,

where large volumes of oil field produced water is generated. Previous subsidence studies conducted by the KCS have identified five areas of interest (AOIs) [Figures 1.2 and 3.26].
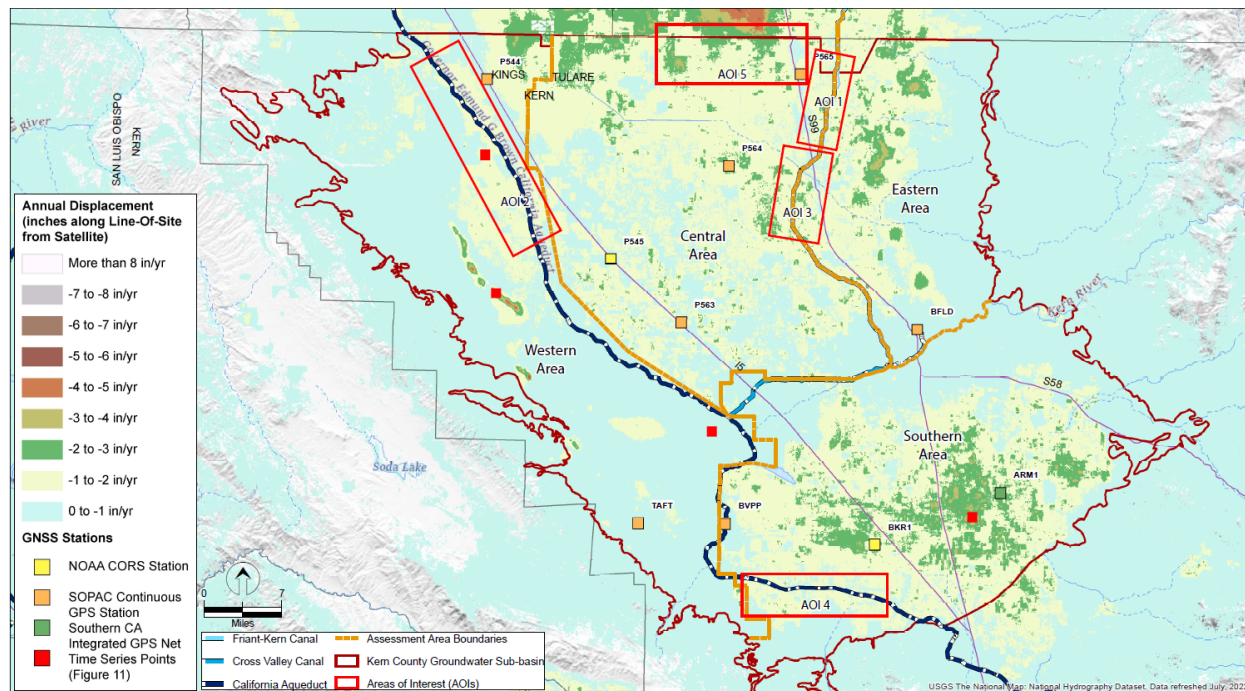

Figure 3.26. The five Areas-of-interest (AOI) of the Kern County Sub-Basin (KCS) that will be discussed in this report.

AOI-1 is located in the eastern side of the KCS along the Canal (Mileposts 120-130). AOI-2 is located on the west side of the KCS adjacent to the Lost Hills Oil field and the California Aqueduct (mile posts 195 to 215). AOI-3 is located on the Canal near Kimberlina Road (Mileposts 130-137). AOI-4 is located in the southern part of the KCS (mile posts 262 to 271) and AOI-5 is located along the northern portion of the KCS where portions of a large subsidence bowl centered to the north of the KCS has expanded into Kern County due to agricultural pumping.

Factors affecting the groundwater recharge in the KCS include the topography surrounding the sub-basin boundary, which is generally mountainous to the west, south and east of the basin Figure 3.27. Additionally, the west side of the KCS is distinguished by geologic folding which impedes groundwater flow, alkali soils, and extensive oil extraction activities that generate significant volumes of exempt produced water from some of the same formations used for agricultural supply in the sub-basin (e.g., Tulare and Etchegoin Formations). Another
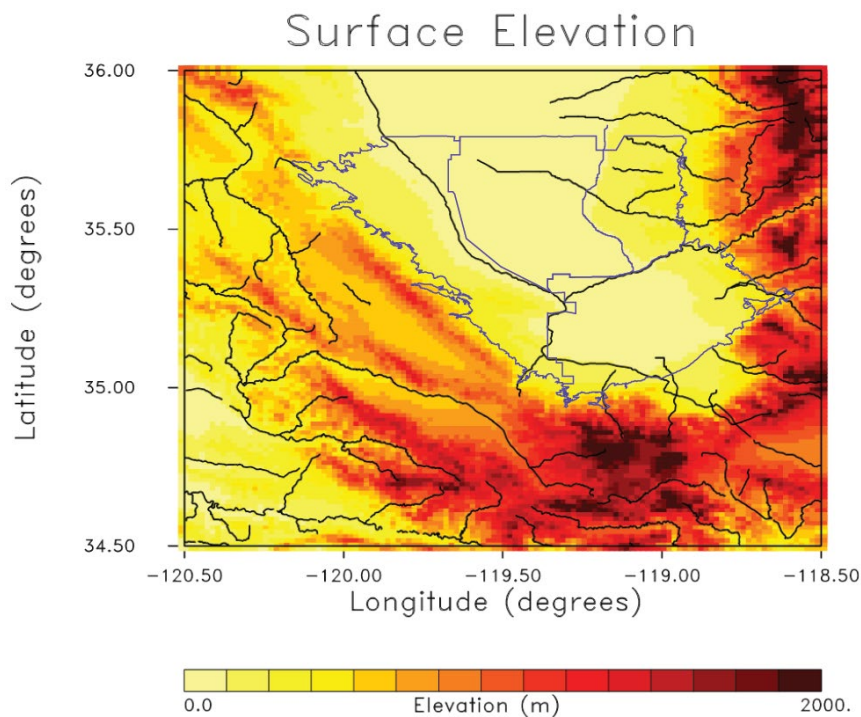
Figure 3.27. Topography surrounding the Kern County Sub-Basin.

important element is the extent and depth of the Corcoran Clay within the sub-basin as changes in effective transmissivity within the confined aquifer below the clay can produce considerable subsidence. The Corcoran Clay underlies most of the sub-basin (Figure 3.28) with some notable exceptions (e.g., west side and Kern fan). These include near and on the anticlinal structures common to the west side where the Corcoran thins or is absent, and the area west of the anticlines were a discontinuous clay identified as being equivalent to the Corcoran Clay is present. East and towards the axis of the KCS there are parts of the sub-basin where the clay lies at depths of around 275 m (~902 ft.). The average depth of the Corcoran Clay within the KCS is 111.6 m (~366 ft.), the minimum depth to the clay is 54 m (~177 ft.).
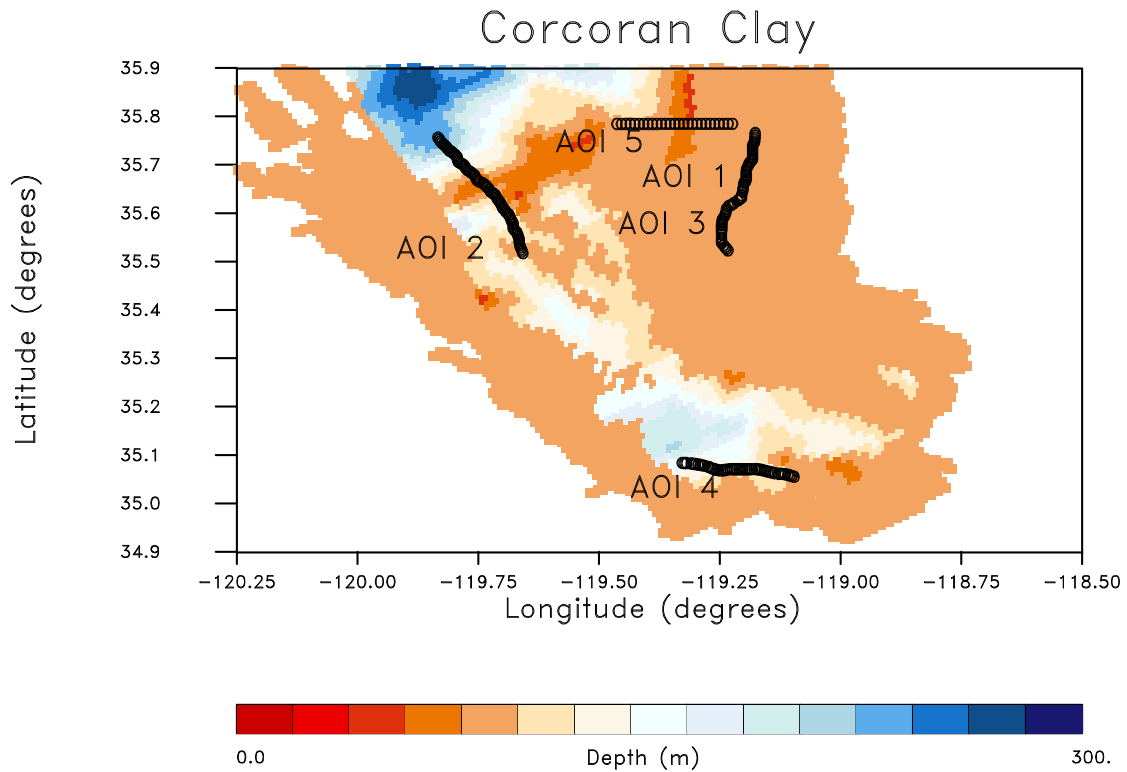
Figure 3.28. Depth to the top of the Corcoran Clay layer. The lines indicate the locations of the five areas of interest (AOIs).

For the San Joaquin Valley and the KCS as a whole, areas that are most susceptible to subsidence appear to be regions where there is a high density of wells penetrating fine-grained sediments such as the Corcoran Clay and extending into the lower confined aquifer. Thus, it is beneficial to examine those regions in the KCS that have higher densities of agricultural wells reaching below the Corcoran Clay. In Figure 3.29 we plot well densities and find a higher density of wells below the Corcoran Clay at the east-central edge of the valley. In one portion of this region the Corcoran Clay is rather shallow, making well penetration more likely. As noted previously, on the west side and on the Kern fan, clays are either thin, discontinuous, or absent. There is also extensive withdrawal of non-SGMA water, extracted as part of the oil production process on the west side. This exempt water, referred to as "produced water", is entrained with the oil. The California Geologic Energy Management (CalGEM) Division reports volumes of produced water for oilfields in California. In the KCS, the ratio of barrels of produced water to barrels of oil is often in excess of 10:1.
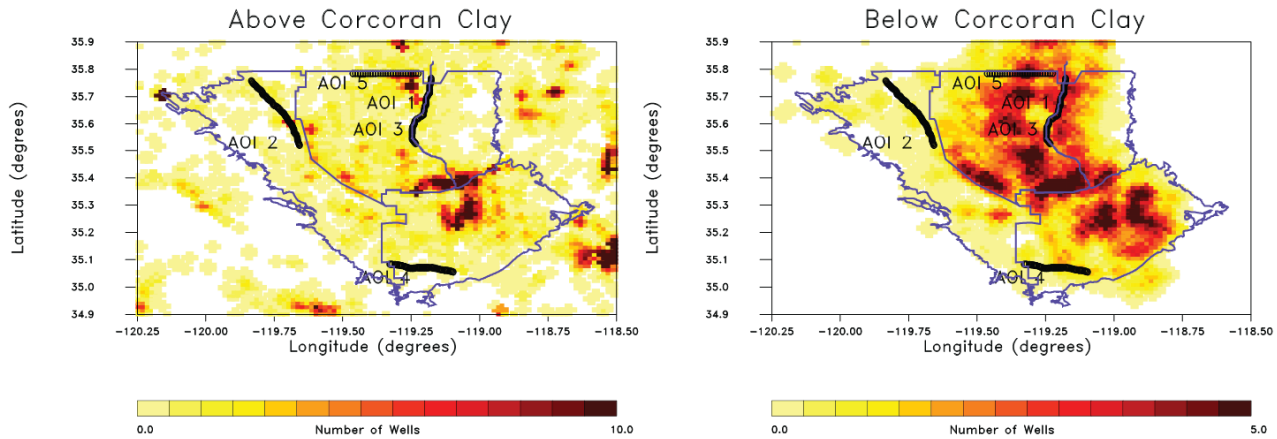
Figure 3.29. Densities of wells that end (Left) Above the Corcoran Clay and (Right) Below the Corcoran Clay.

Figures 3.30 through 3.36 are plots of the KCS LOS displacements for the six one-year time intervals from 2016 until 2021.
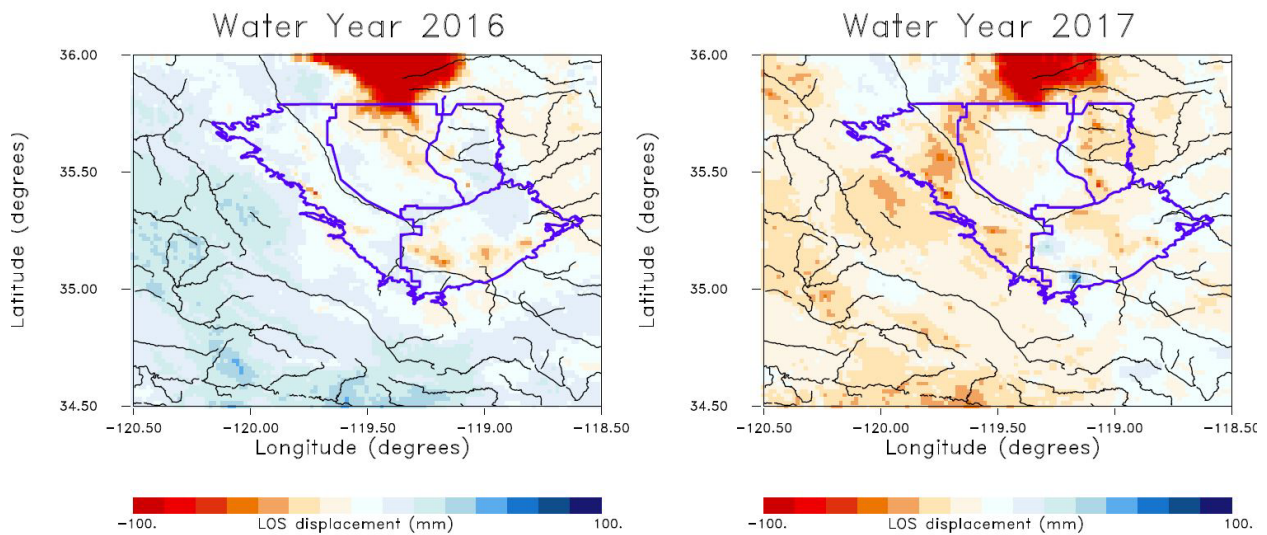

Figure 3.30. KCS line-of-sight displacements for water years 2016 (Left) and 2017 (Right). The lines denote the major rivers and streams in the region including the California Aqueduct which is labelled Aqueduct.

The southern edge of the large-scale subsidence originating north of the (AOI-5) seen earlier in Figures 3.13 and 3.30 is visible at the top of Figure 3.34.
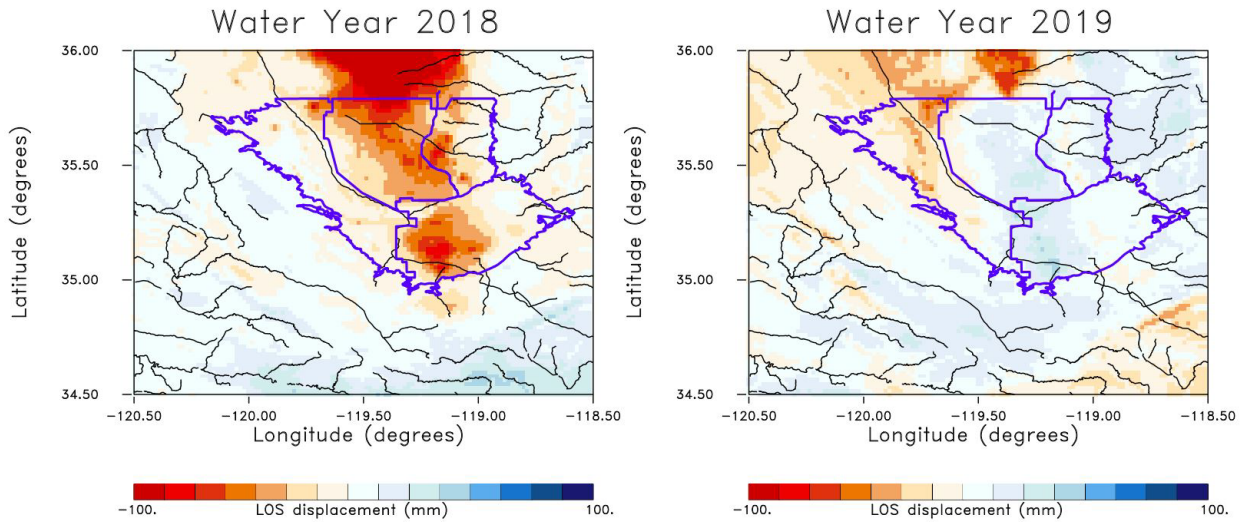
Figure 3.31. Line-of-sight displacements for the water years 2018 (Left) and 2019 (Right).
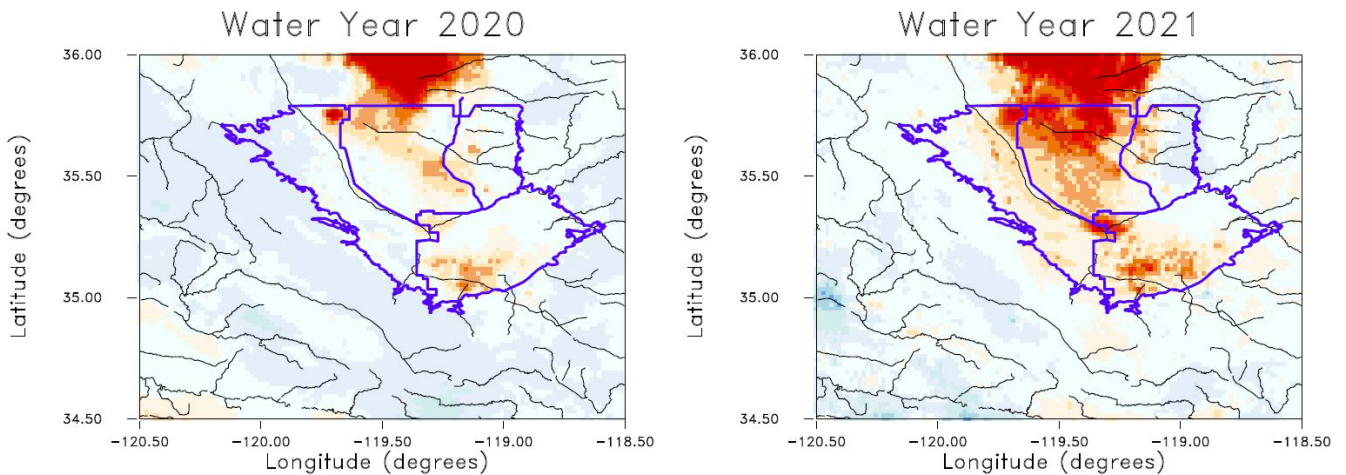
Figure 3.32. Line-of-sight displacements for the water years 2020 (Left) and 2021 (Right).

The long-term subsidence in AOI-5 at the northern edge of the KCS is evident in all of the years plotted. The water year 2019 has the clearest evidence of rebound in the KCS during a wet year, the rebound in 2017 is very localized. Excluding surface water banking activities, the subsidence in 2018 and 2021 have the clearest correlation to groups of wells extending below the Corcoran Clay in the central portion of the KCS (i.e., AOIs 1, 3, and 5).

Another factor influencing subsidence is the fraction of fine-grained sediments, the amount of clay in particular, that is found in areas subject to fluid withdrawal. As indicated by the Helm model (1975, 1976) the clays undergo

inelastic compaction when the effective pressure is reduced below the historic minimum. Compressibility of fine-grained sediments are typically several orders of magnitude greater than compressibility of coarse-grained sediments (Sneed, 2001). Therefore, this study utilized the USGS sub-basin textural model of Faunt (Faunt et al. 2010) to calculate the fraction of coarse-grained sediments above and below the Corcoran Clay. The greatest subsidence is expected to occur when fine-grained sediments coincide with a concentration of wells drilled into the lower confined aquifer. The coarse fractions above and below the Corcoran Clay are plotted in Figure 3.37. There are generally fine sediments below the Corcoran clay, with a coarse fraction that is less than 50%.
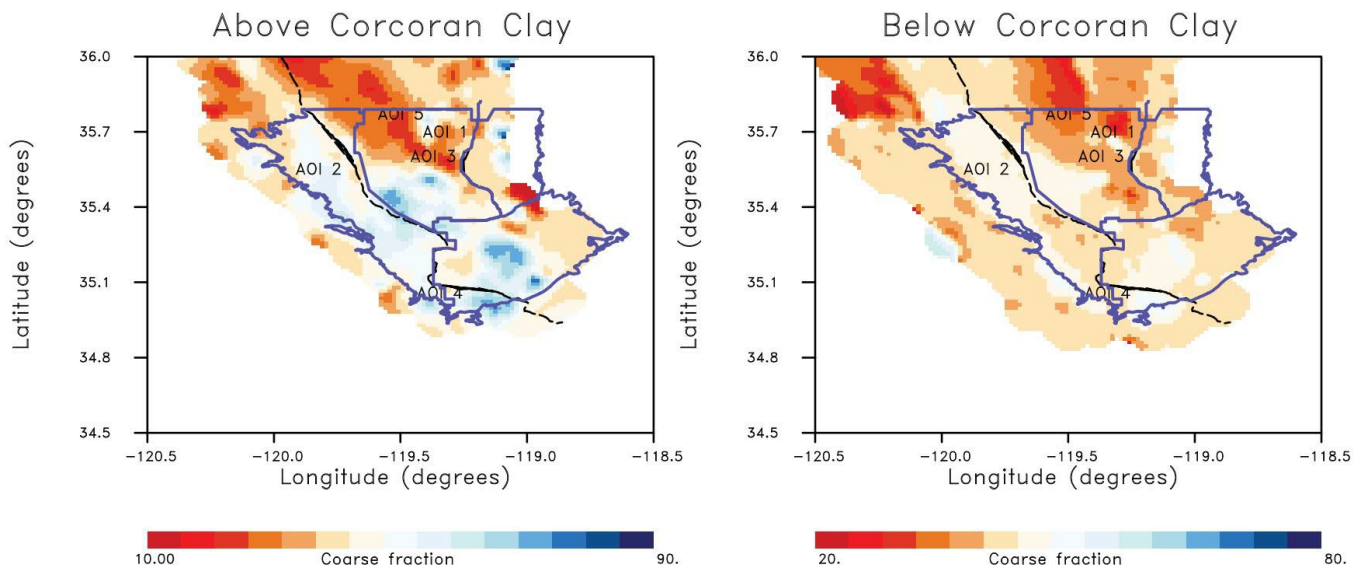
Figure 3.33. (Left) Coarse sediment fraction above the Corcoran Clay layer. (Right) Coarse sediment fraction below the Corcoran Clay layer. The five areas of interest are labelled, and the dashed line indicates the path of the California Aqueduct. AOI-1 and AOI-3 form a segment of the Friant-Kern Canal identified as subsiding.

The inversion results for volume changes in the upper and lower aquifers was already discussed above. Here we
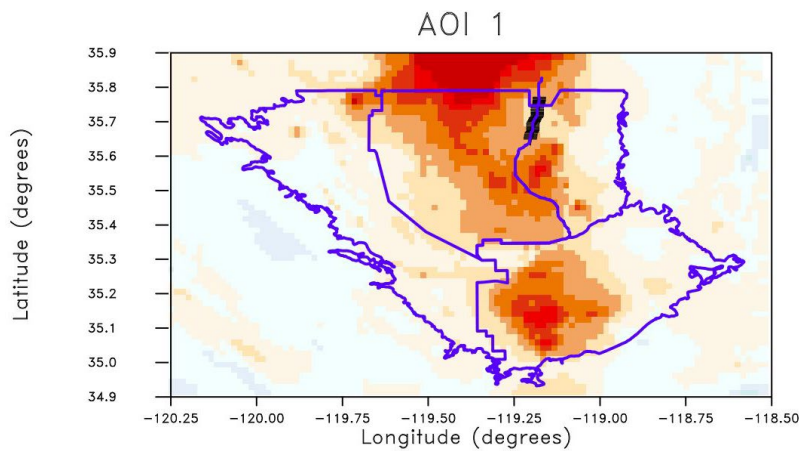

Figure 3.34. The points defining AOI-1, a segment of the Friant-Kern Canal between MP 120-130. The color variations denote the LOS for the water year 2018.

are presenting estimates of displacements for the five areas of interest, that is along the lines plotted in Figure 3.28. We now discuss the displacements in each area interest in succession, beginning with Area-of-interest 1 (AOI 1), a segment of the Friant-Kern Canal between mile posts 120 and 130.

First, we compare the LOS displacement measured by the InSAR Sentinel 1A/B satellites to the calculated vertical displacement based upon the inversion result. The inversion result was able to match the observed LOS measurements.
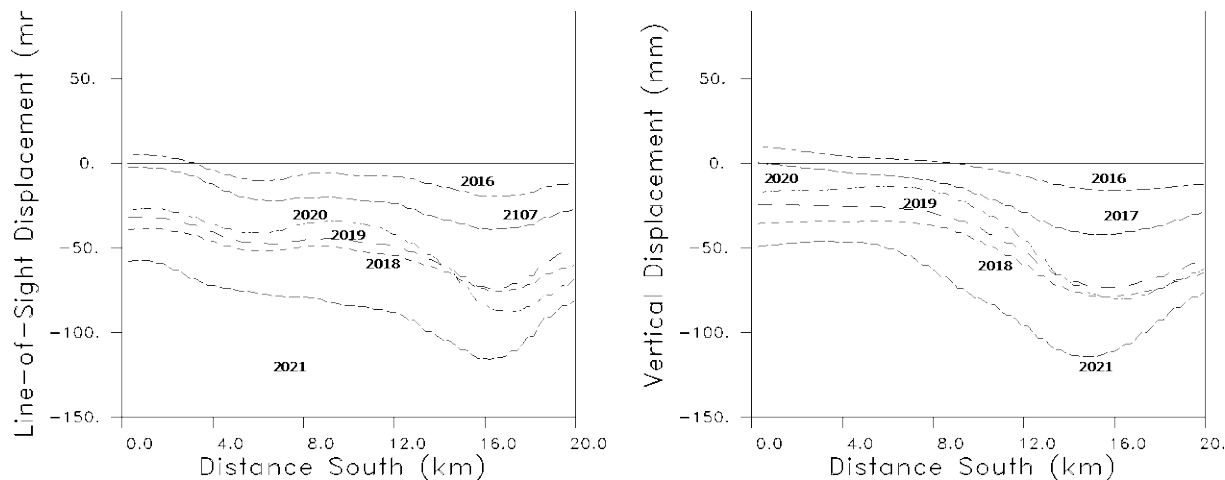
Figure 3.35. (Left) Line-of-sight displacements for the line in AOI 1, as observed by the Sentinel 1A/B satellites. (Right) Vertical displacements using the aquifer volume change models to calculate the three-dimensional displacements.

The deformation due to relatively shallow aquifer compaction is dominated by vertical displacements, such as those shown in Figure 3.35. However, there are also horizontal displacements, and these can be damaging for
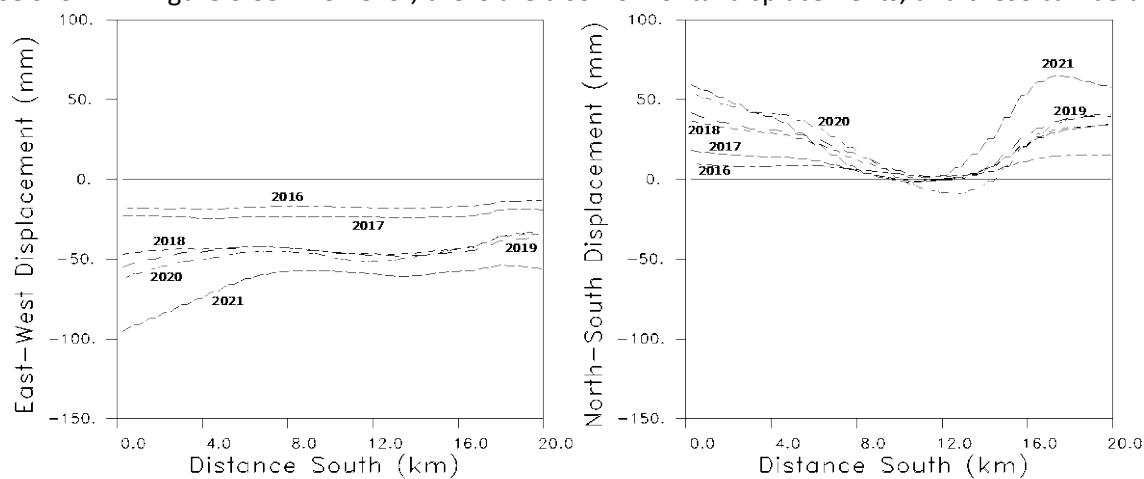

Figure 3.36. East-west (left) and north-south (right) displacements calculated for the path of the Friant-Kern Canal in AOI-1.

linear critical infrastructure. Figure 3.36 plots the east-west and north-south horizontal displacements for the curve in AOI- 1 (Figure 3.34).

The peak horizontal displacements of 10 cm (~4 inches) from 2015 to 2021 are of the same order as the vertical displacements plotted in Figure 3.35. Due to the expansion of the subsidence bowl to the north, the Aqueduct may be displaced relatively uniformly to the east.
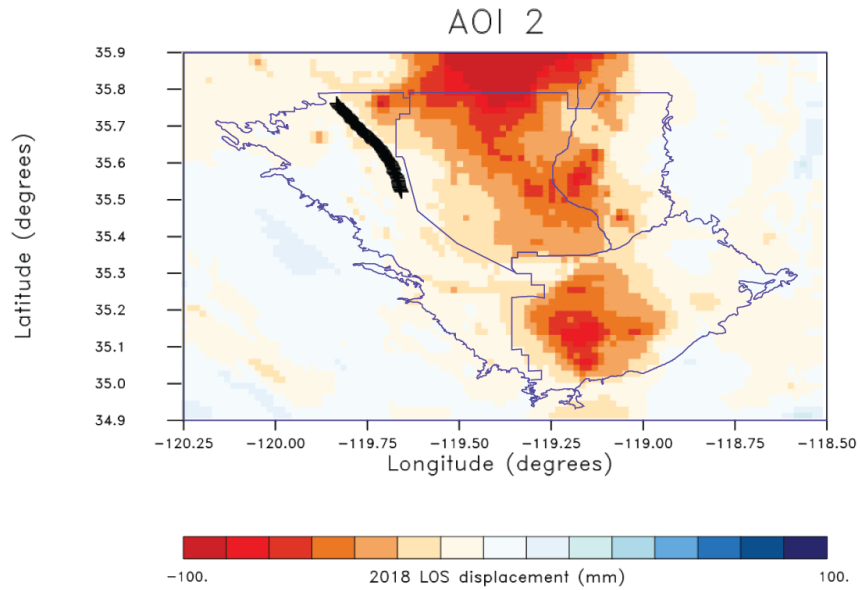

Figure 3.37. AOI-2, a segment of the Aqueduct between mile posts 195-215. The points on the path are plotted on top of an image of the LOS displacement in water year 2018.

The second area-of-interest (AOI 2) is a segment of the California Aqueduct between mile posts 195 and 215 that
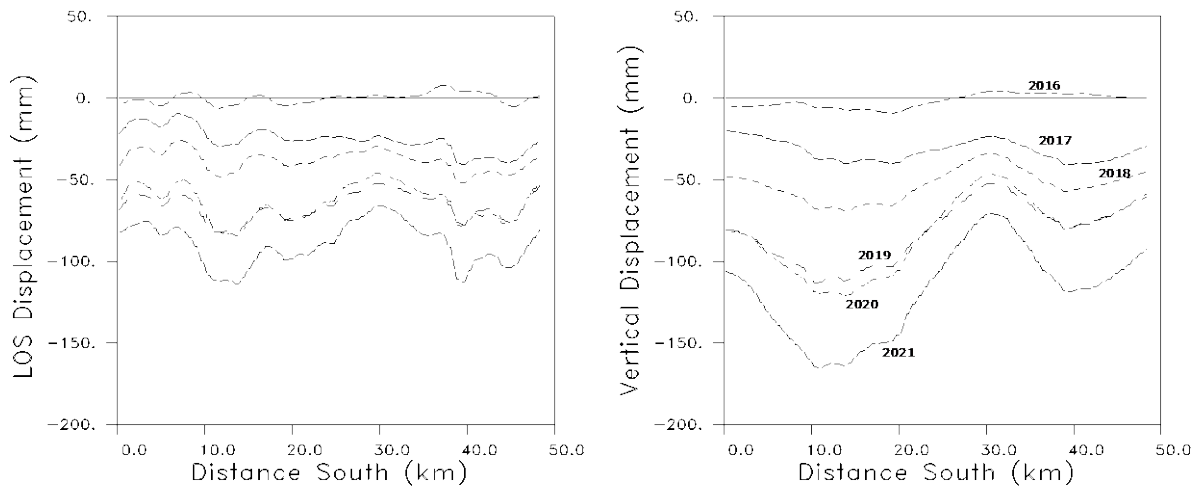

Figure 3.38. AOI-2 along the California Aqueduct. (Left) Line-of-sight displacement for yearly intervals from 2015 to 2021. (Right) The corresponding vertical displacement calculated using the volume change model that resulted from an inversion of the InSAR data.

is near the northwestern edge of the KCS and adjacent to the Lost Hills Oilfield (Figure 3.37) where the subsidence from non-SGMA-related activities is a likely source of deformation that is likely impacting critical infrastructure. The Sentinel observed LOS displacements and the estimated vertical deformation for this segment of the Aqueduct is plotted in Figure 3.38.

The horizontal displacements calculated using the aquifer volume change model are shown in Figure 3.39.
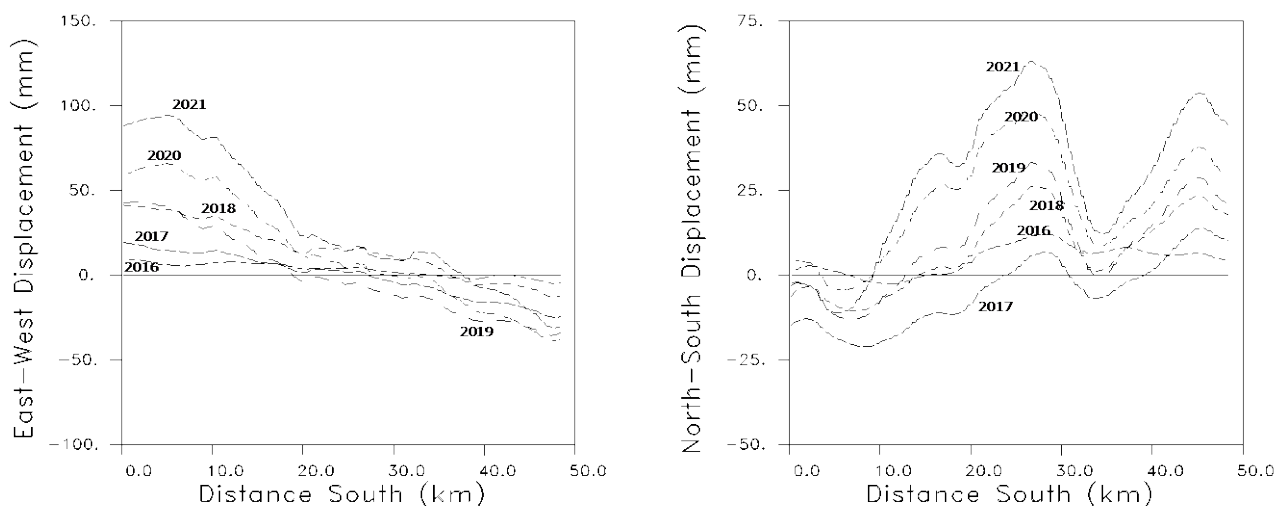

Figure 3.39. (Left) East-west and (Right) north-south displacements in AOI 2, calculated using the aquifer volume change models plotted in Figures 3.18-3.24.

The peak horizontal displacements of around 10.0 cm (~4 inches) are smaller than the over 15.0 cm (~6 inches) of vertical displacement (Figure 3.38). The northern edge of the Aqueduct is likely moving rapidly eastward,
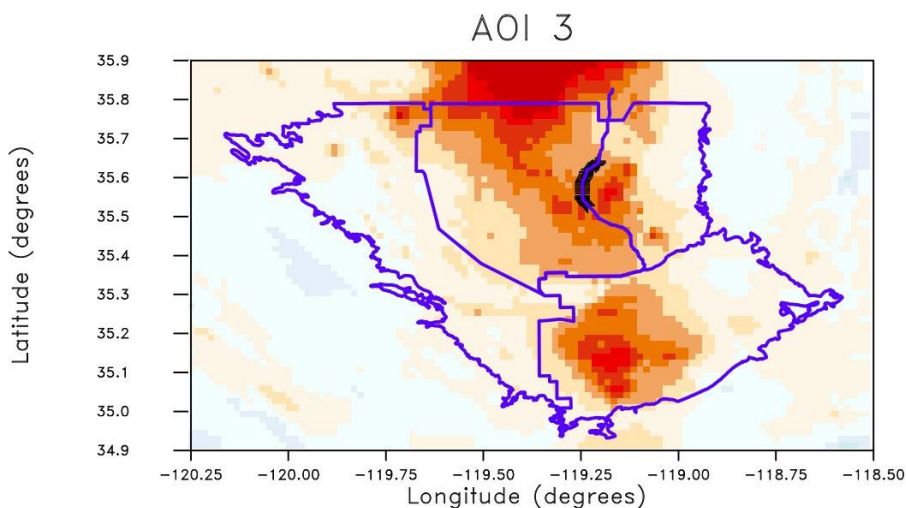

Figure 3.40. AOI-3, the segment of the Friant Kern Canal between mileposts 130 and 137.

deformation caused by oil extraction activities at Lost Hills Oil Field where fluids, including produced water, are being withdrawn from the limbs of the anticline as a result of oil pumping along the crest.

Area-of-interest 3 is the of the Friant Kernel Canal between mile posts 130 and 137, plotted in Figure 3.40. The LOS displacement and the calculated vertical displacements are shown in Figure 3.41.
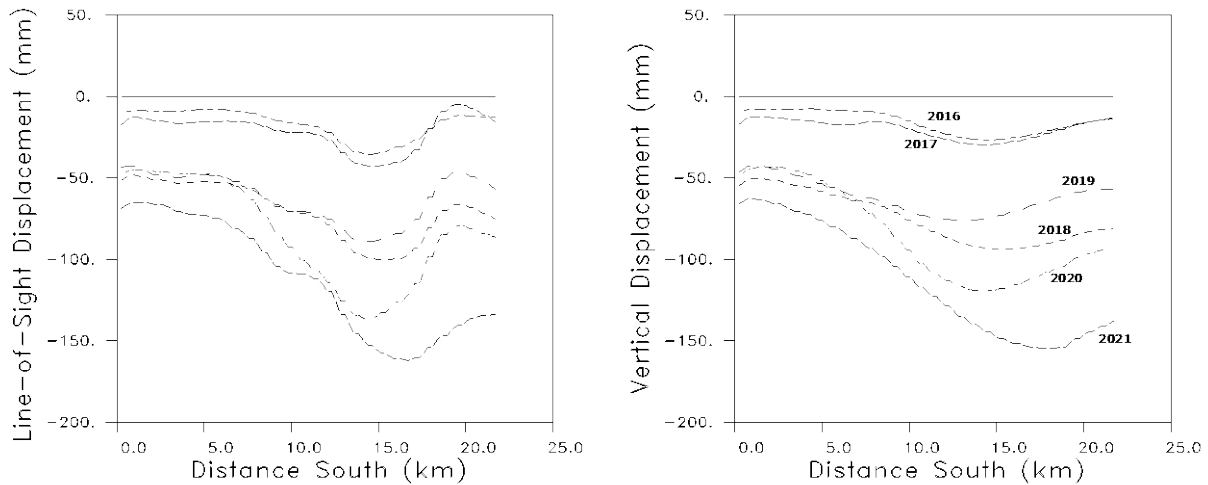

Figure 3.41. (Left) Line-of-sight displacements and calculated vertical displacements from 2015 to 2021, plotted in one-year increments.

From 2015 to 2021 there has been over 15 cm (~6 inches) of cumulative displacement, with peak displacements at the southern end of the segment. The calculated horizontal displacements are shown in Figure 3.42.
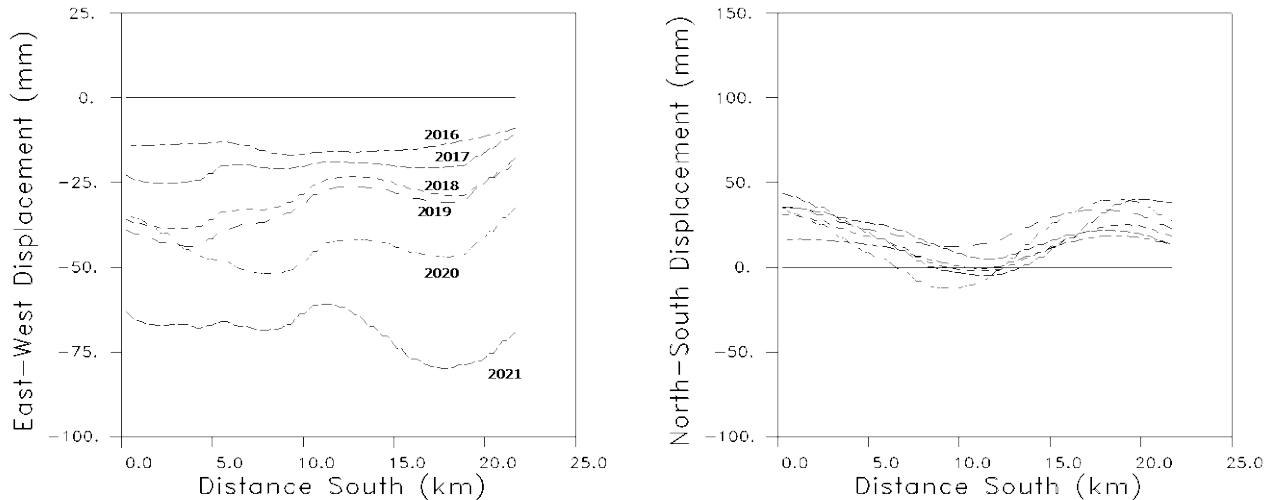

Figure 3.42. (Left) East-west and (Right) north-south displacements along the Friant-Kern Canal segment in area-of-interest 3.

The horizontal displacements are about one-half of the magnitude of the vertical displacements, less than 10 cm (4 inches) over the six-year interval. The north-south displacements are under 5 cm (~2 inches) in magnitude.

To assess subsidence, the Friant Water Authority and USGS are installing a new extensometer and monitor wells in AOI-3 adjacent to the Canal near Kimberlina Road.

AOI-4 is a southern segment of the California Aqueduct (MP 262-271) that runs roughly east-west at the southern edge of the KCS. Based on previous studies by the KCS the likely cause of subsidence in this area is a combination of agriculture and oil-related activities. As can be seen in Figures 3.30-3.32 the area is subject to a complicated pattern of displacements, likely due to the complex hydrodynamics and converging drainage patterns from the south and eastern edges of the basin and the combination of extraction activities. The geometry of the segment is shown in Figure 3.43.
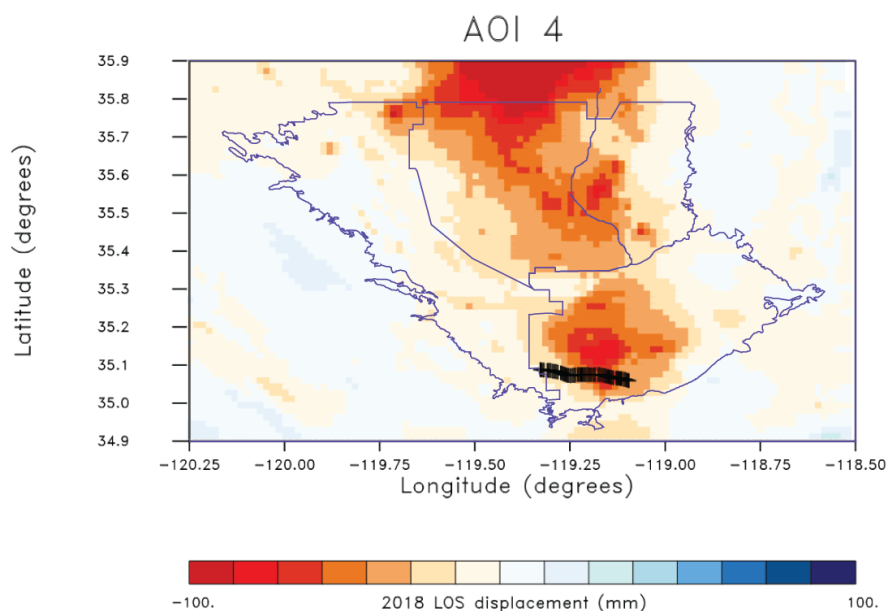

Figure 3.43. Area-of-interest 4, a southern segment of the California Aqueduct between mile posts 267-271

The line-of-sight and vertical deformations are plotted in Figures 3.44 and 3.45. There is significant upward movement (recovery) in 2017 and 2019, and subsidence in 2018, 2020, and 2021. The area seems subject to greater variability in displacements in comparison to central regions of the KCS north of the Kern River.
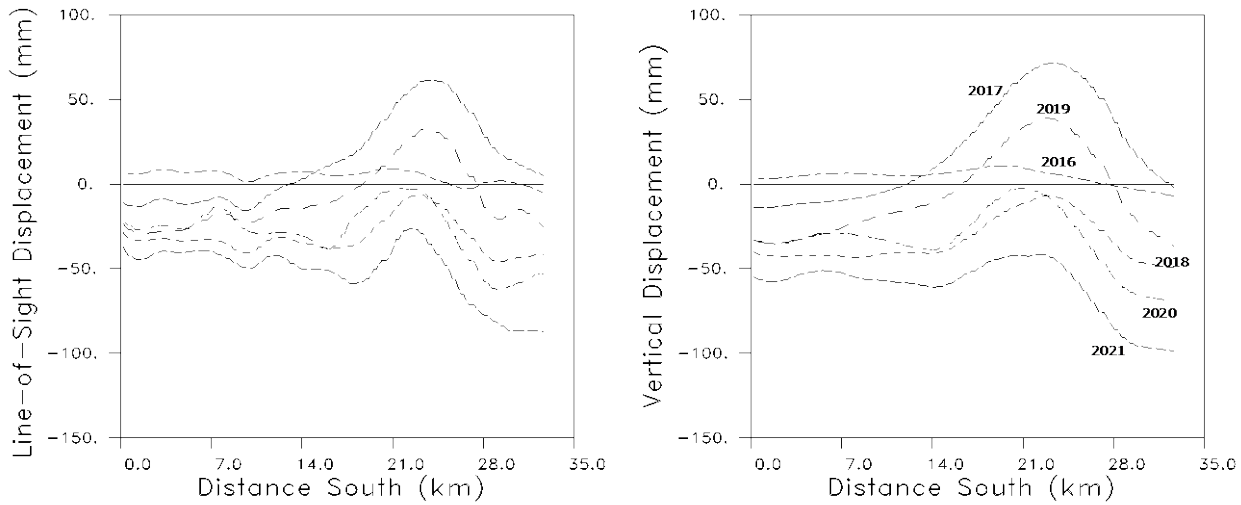
Figure 3.44. (Left) Observed LOS displacement and Figure 3.45 (Right) calculated vertical displacements for AOI- 4, a segment of the southern California Aqueduct between mile posts 267 and 271, shown in Figure 3.43.

Horizontal displacements, calculated using the models obtained by inverting the InSAR observations, are plotted in Figure 3.46. The north-south displacements are of the same order as the vertical displacements, around 10 cm (~4 inches), indicating substantial horizontal motion.
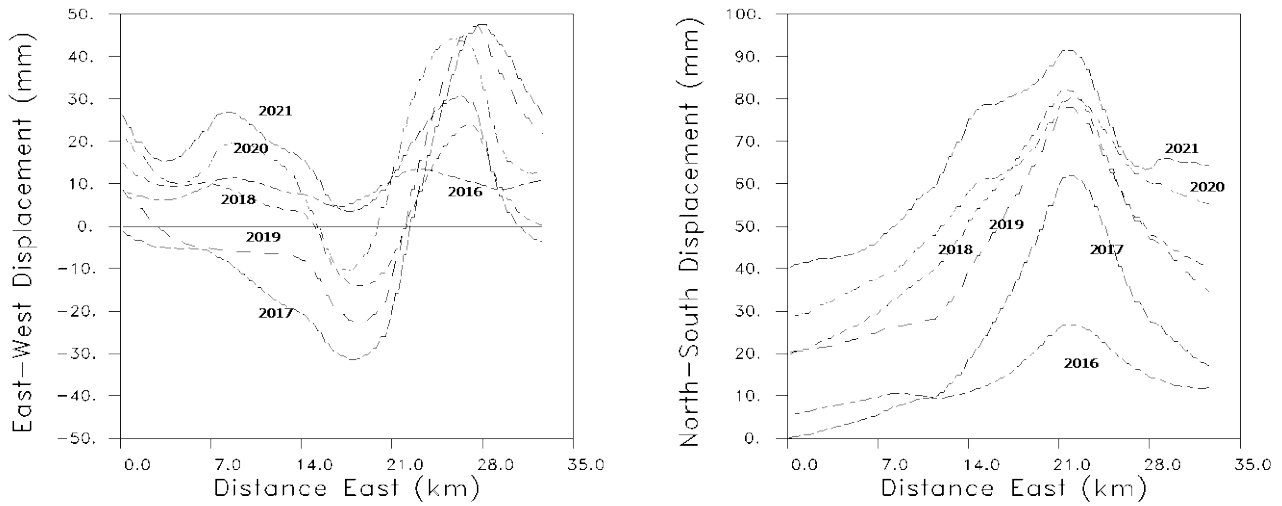

Figure 3.46. AOI- 4. (Left) East-west and (Right) north-south displacements calculated using the models shown in Figures 3.18-3.24, obtained by inverting the InSAR line-of-sight data.

AOI 5, shown in Figure 3.47, lies on the northern boundary of the KCS. This area is a jurisdictional boundary and is not hydraulicly controlled. The data shows that AOI-5 is strongly influenced by the major subsidence bowl to
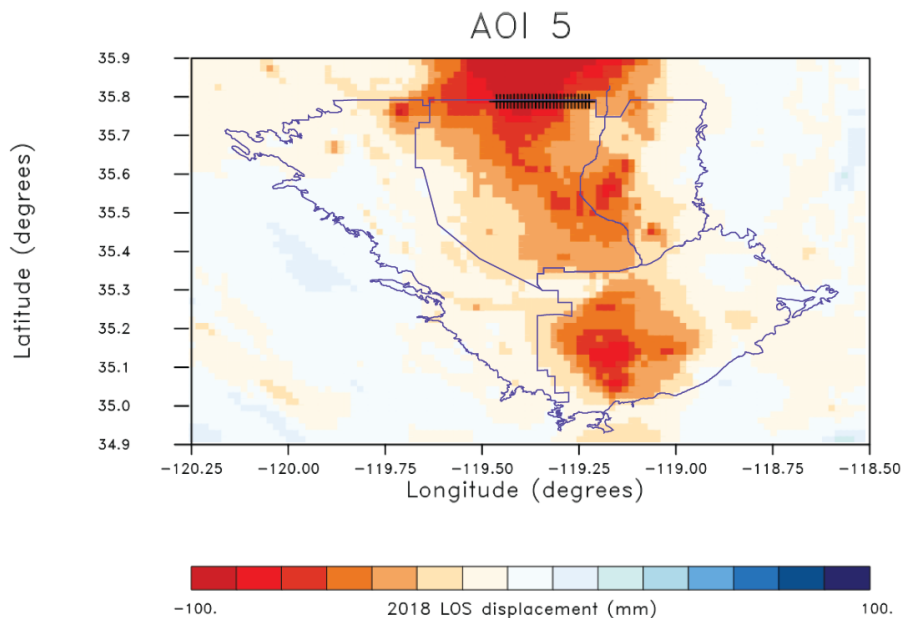

Figure 3.47. AOI-5, a segment of the northern boundary of the Kern County Sub-Basin.

the north of Kern County, centered near the towns of Alpaugh and Corcoran.

The line-of-sight (LOS) displacements recorded by the Sentinel InSAR satellites are plotted in Figure 3.48, along with the vertical displacements calculated using the models of aquifer volume change obtained by inverting the LOS data.
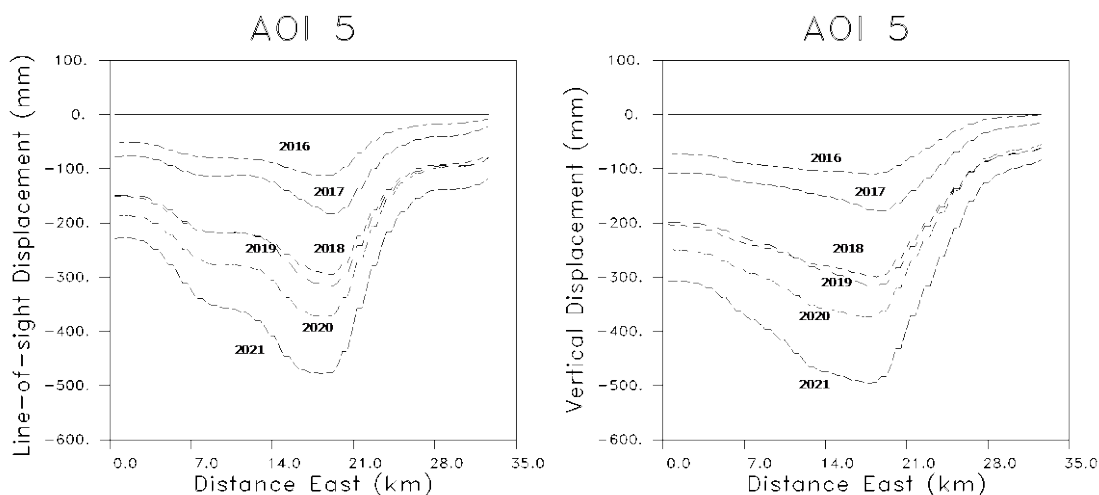

Figure 3.48. (Left) LOS displacements in AOI-5, on the northern edge of the KCS. (Right) Calculated vertical displacement for the points along the path shown in Figure 3.47.

The vertical displacements in this area are among the largest in the sub-basin, approximately 0.5 meters (~1.6 ft.) of cumulative subsidence between 2015 and 2021. Similarly, the horizontal displacements in the region are quite large with a peak displacement of around 30 cm (~ 11.8 inches) (Figure 3.49).

Figure 3.49. Horizontal displacements in AOI 5.
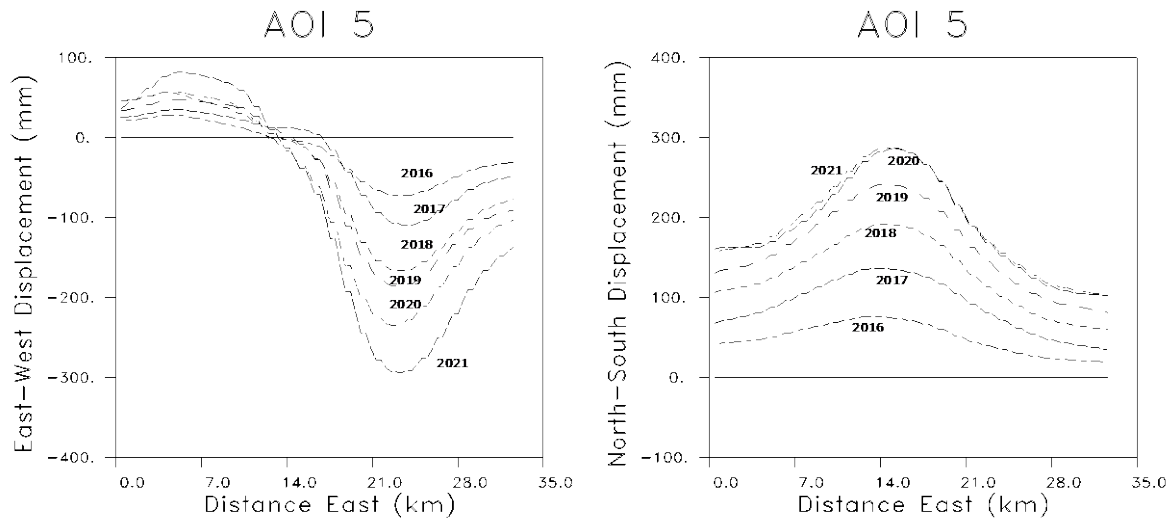
Thus, horizontal displacements can be significant in the KCS and may impact local and regional critical infrastructure. Therefore, horizontal displacements should be considered when planning future infrastructure rehabilitation and subsidence monitoring programs. GPS observations should help in this regard, particularly when augmented with InSAR satellite-based LOS data.

4. Location of Ground-Based Geodetic Devices.

Inelastic aquifer compaction, leading to land subsidence, has been identified as an undesirable result due to groundwater extraction. Factors that bear on the degree of subsidence are: local geotechnical conditions (e.g., soil type, construction practices, etc.), infrastructure age, groundwater usage, and nearby non-SGMA-related activities. The deformation data discussed in this study exhibits a strong correlation between displacements and drought years pointing to the effects of groundwater usage and changes in soil moisture, such as those identified
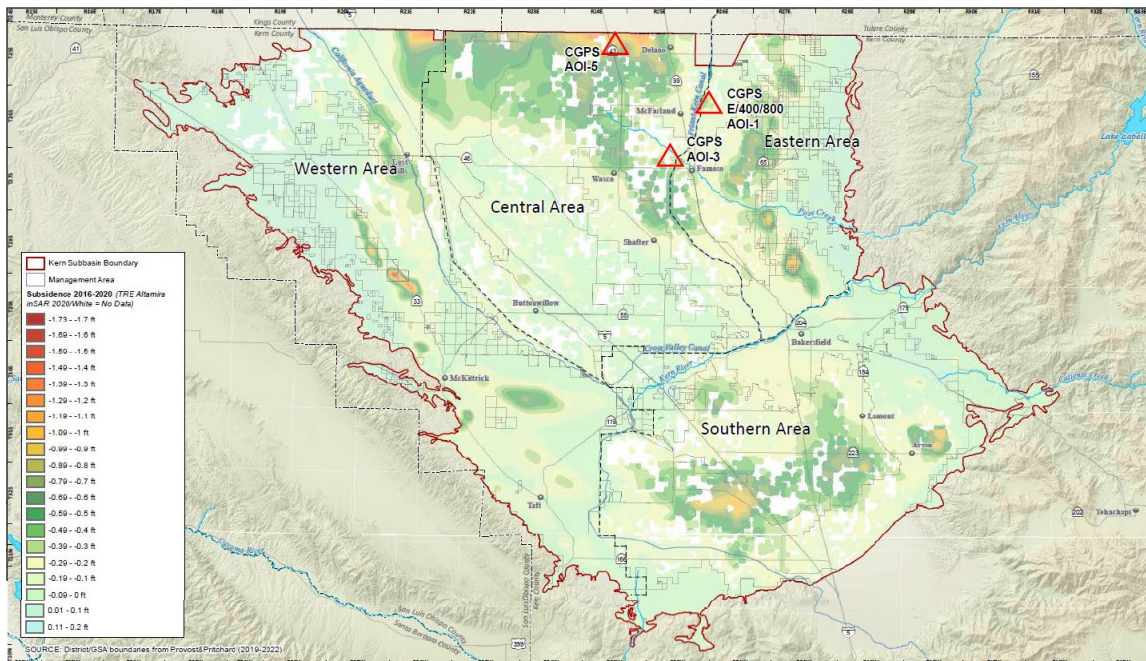

Figure 4.1. Proposed locations of the three continuous GPS stations in areas-of-interest 1, 3, and 5. The color variations denote the 2016-2020 subsidence. Figure from Aquilogic report 'KCS Subsidence Friant-Kern Canal Monitoring Recommendations, 2022'.

in the Central Region. There also seem to be areas of elastic rebound during wet years, visible in Figures 3.34 and 3.35. However, there are a significant number of oil fields in the KCS which produce in a continuous, non-seasonal pattern of subsidence. This distinction was illustrated in a differential InSAR study conducted by Earth Consultants International (ECI) on behalf of the KGA (ECI, 2021). Thus, the temporal sampling of the GPS observations, often hourly, in conjunction with InSAR, is advantageous in further delineating the source of subsidence and distinguishing SGMA-related groundwater-related pumping effects from other non-SGMA sources, such as oil field activities. Furthermore, we have seen that the surface deformation may contain significant horizontal motion and the full three-dimensional displacement field, which is provided by GPS, should be measured and evaluated. Note that InSAR observations will still be necessary, as there are several areas of concentrated deformation, as shown in Figure 4.1. We have also seen how deformation shows a good correspondence with
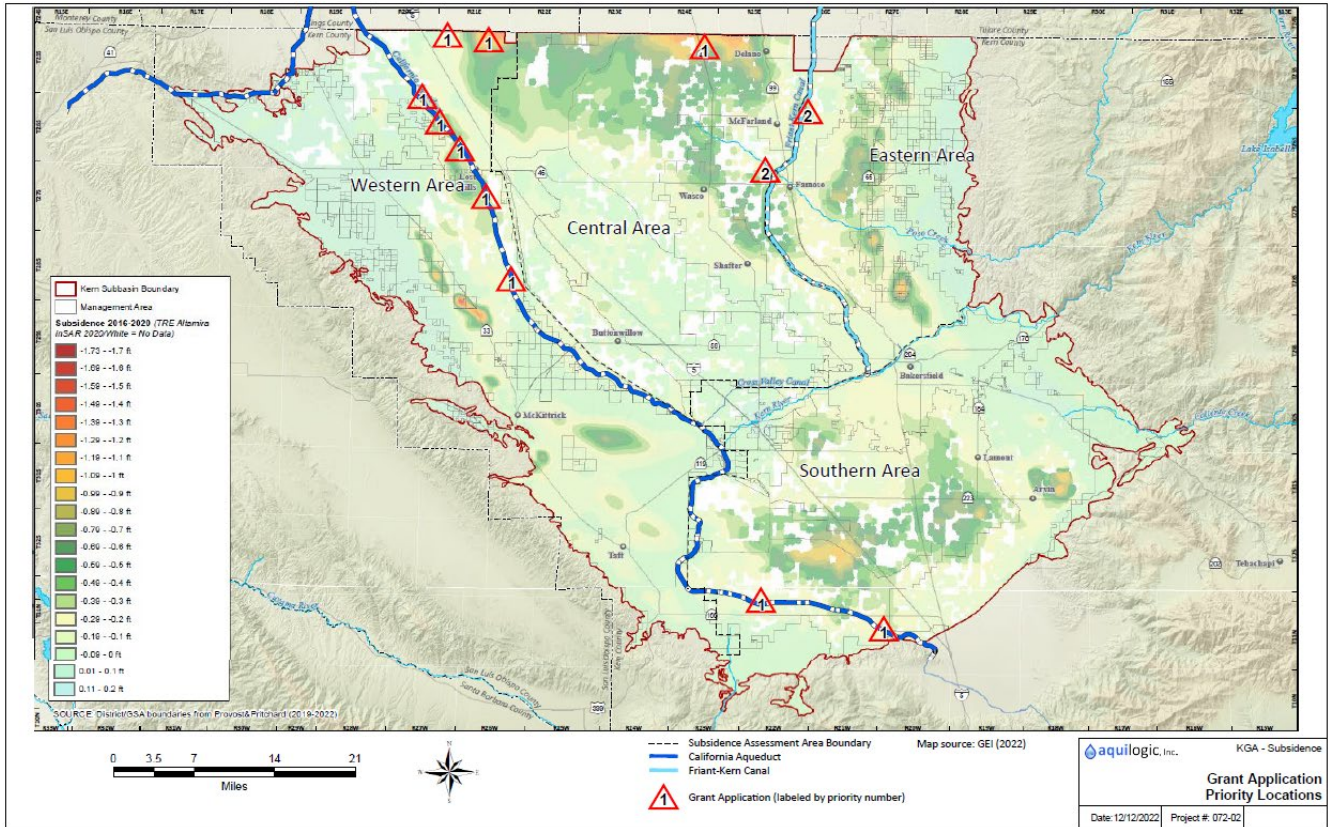
Figure 4.2. Location of proposed monitoring infrastructure to be added.

Wells that penetrate into the deeper confined aquifer below the Corcoran Clay, particularly in the Central Region of the KCS. Therefore, monitoring the deformation and effective pressure changes at depth will refine our understanding of the exact sources of the subsidence and potentially suggest avenues for mitigation. Additional instrumentation that will complement existing monitoring networks are continuous Global Positioning System (cGPS) instruments, dedicated dual completion monitoring wells, and extensometers completed so as to monitor shallow and deeper compaction. The five AOIs in the KCS identified for in-depth analysis were discussed elsewhere in this report. AOI's 1, 3, and 5 are located in the north-east corner of the sub-basin as shown in Figure 4.1. The KCs recently was awarded State grant funding to install dual depth extensometers along the Canal in AOI 3. A location near Kimberlina Road in the KGA was selected in consultation with the Friant-Kern Water Authority and the USGS for installation of the extensometer and associated monitoring wells. The extensometers will be installed in cooperation with the USGS in September of 2023. A location along Peterson Road adjacent to the Canal in AOI-1 is also proposed for future monitoring. The KCS has submitted an application for additional equipment for AOI-1, AOI-2, and AOI-5.

As noted above, considerable horizontal deformation is estimated for these areas, based upon the inversion results. Therefore, additional continuous GPS stations located here can help calibrate and validate the InSAR estimates of three-dimensional displacements.

AOI-2 is an approximately twenty-mile-long segment of the California Aqueduct (Figure 3.37) that includes Mileposts 195 to 215. This reach of the Aqueduct is subject to displacements related to non-SGMA-related
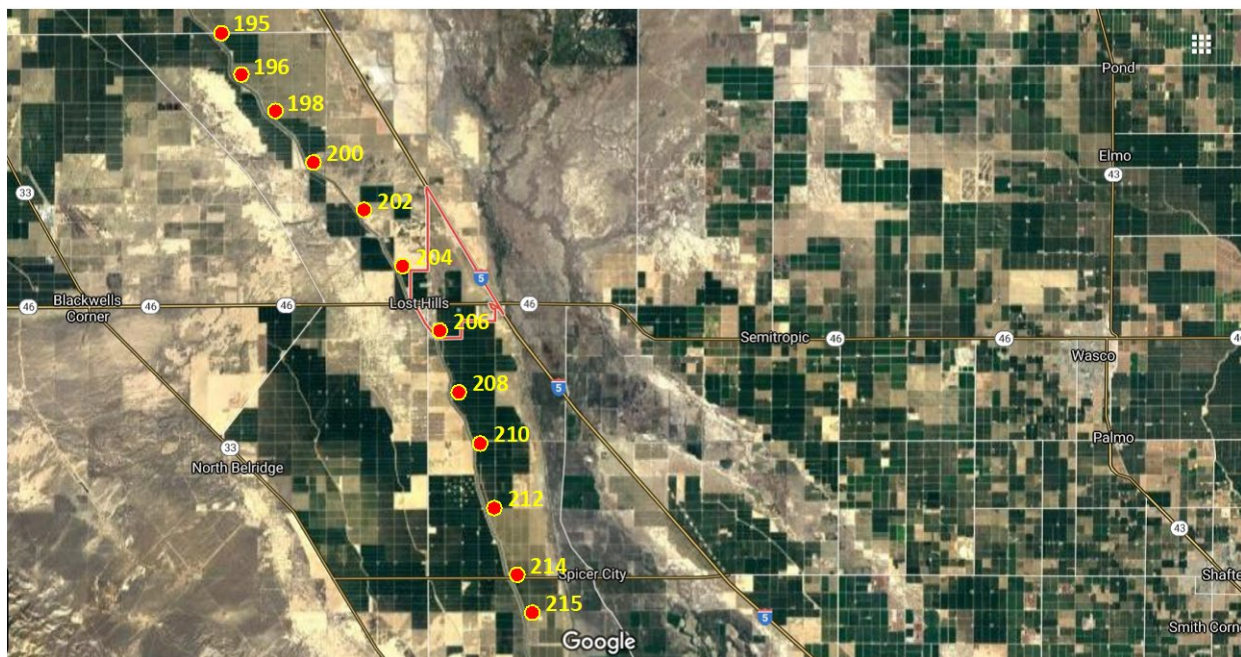

Figure 4.3. Milepost markers along the California Aqueduct. The Lost Hills oil field is the bare ground to the west of the aqueduct and extends from approximately milepost 195 to 215. Figure from Aquilogic report 'KCS Subsidence California Aqueduct Monitoring Recommendations, 2022'.

activities (e.g., geotechnical and the Lost Hills oil field just to the west). In order to refine existing data, it is proposed to collect measurements of the three-dimensional displacements at or near the Aqueduct. To gather this data the KCS has proposed a network of GPS stations, monitor wells, and extensometers. (Figure 4.3). As for AOI's 1, 3, and 5, the proposed monitoring methods are primarily continuous GPS stations, monitoring wells, and extensometers with dual completions at approximately 400 and 800 feet or deeper. If funded by the DWR, this equipment will provide valuable data for the evidence of undesirable results related to subsidence. The proposed additions for the improved monitoring of the Aqueduct starting at the northern edge of the segment in AOI 2 in pools 20-23. In total, the KCS has proposed five continuous GPS stations, four dual-depth extensometers (~400 ft and 800 ft. or deeper) and three sets of co-located monitor wells (~400 ft and 800 ft or deeper). In AOI-4 the KCS has proposed two GPS stations and an extensometer set (i.e., shallow and deep).

6. Conclusions.

This detailed look across the broad range of gravity, InSAR, GPS, water table, borehole, textural, and geological data provides some preliminary conclusions regarding the factors that contribute to subsidence in the KCS:

- Subsidence and inferred reservoir volume change correlate with locations where a greater density of wells penetrate the Corcoran Clay and access the lower confined aquifer.
- Non-SGMA-related activities (e.g., geotech, soils, age of the infrastructure, west side oil, etc.) are a significant contributing factor to subsidence in the KCS, especially where these activities are concentrated near the Aqueduct.
- Models where there is a strong correlation between wells and volume change in the confined aquifer fit the observed line-of-sight displacement well.
- Regions displaying the greatest subsidence (e.g., Central Region) contain a greater proportion of fine-grained sediments in the lower aquifer, in agreement with the conclusion that the inelastic aquifer compaction in clay-rich layers is the greatest contributor to subsidence.
- Subsidence generally related to SGMA-related activities is observed in AOIs 1, 3, and 5. Subsidence in AOI-4 appears to be a mixture of SGMA- and non-SGMA-related activities. In AOI-2, subsidence appears to be primarily related to various non-SGMA-related activities.
- The subsidence rates for the KCS vary. The annual vertical baseline subsidence rates for the individual AOIs are:

AOI-1: 0.50 inches/year, 0.04 feet/year

AOI-2: 0.78 inches/year, 0.07 feet/year

AOI-3: 0.75 inches/year, 0.06 feet/year

AOI-4: 0.40 inches/year, 0.03 feet/year

AOI-5: 2.15 inches/year, 0.18 feet/year

The estimated horizontal displacement associated with surface deformation in the individual AOIs are:

AOI-1: 0.42 inches/year, 0.04 feet/year

AOI-2: 0.21 inches/year, 0.02 feet/year

AOI-3: 0.45 inches/year, 0.04 feet/year

AOI-4: 0.10 inches/year, 0.01 feet/year

AOI-5: 1.24 inches/year, 0.10 feet/year

New high-resolution airborne electromagnetic (AEM) observations collected and utilized in coordination with satellite-based geodetic data, such as GPS and InSAR, will help refine future study estimates. Furthermore, an integrated inversion for both inelastic and elastic aquifer volume changes is feasible. An integrated inversion, along the lines of that conducted in Vasco et al. (2022), would allow for the incorporation of all observations to estimate the residual elastic volume changes that occur from month to month, after the permanent inelastic deformation is removed.

References

Argus, D. F., Martens, H. R., Borsa, A. A., Knappe, E., Weise, D. N., Alam, S., Anderson, M., Khatiwada, A., Lau, N., Peidou, A., Swarr, M., White, A. M., Bos, M. S., Ellmer, M., Landerer, F. W., and Gardiner, W. P., 2022, Surface water flux in California's Central Valley and its source watershed from space geodesy, *Geophysical Research Letters*, **49**, e2022GL099583, https://doi.org/10.1029/2022GL099583.

Bürgmann, R., and Thatcher, W., 2013, Space geodesy: A revolution in crustal deformation measurements of tectonic processes. *Geological Society of America, Special Paper* **500.**

Bock, Y. and Melgar, D., 2016, Physical applications of GPS geodesy: a review. *Reports on Progress in Physics*, **79**, 10, 106801.

Carnec, C., and Fabriol, H., 1999, Monitoring and modeling land subsidence at the Cerro Prieto geothermal field, Baja California, Mexico, using SAR interferometry, Geophysical Research Letters, **26**, 1211-1214.

Dixon, T. H., 1991, An introduction to the Global Positioning System and some geological applications, *Reviews of Geophysics*, **29**, 249-276.

Faunt, C. C., 2009, Groundwater Availability of the Central Valley Aquifer, California, *Professional Paper* **1766**, U. S. Geological Survey, Reston, Virginia.

Faunt, C. C., Belitz, K., and Hanson, R. T., 2010, Development of a three-dimensional model of sediment texture in valley-fill deposits of Central Valley, California, USA, *Hydrogeology Journal*, **18**, 625-649.

Ferretti, A., 2014, *Satellite InSAR Data – Reservoir Monitoring from Space*. EAGE Publications.

Ferretti, A., Fumagalli, A., Novali, F., Prati, C, Rocca, F., and Rucci, A., 2011, A new algorithm for processing interferometric data-stacks: SqueeSAR, IEEE Transactions on Geoscience and Remote Sensing, **49**, 3460-3470.

Gabriel, A. K, Goldstein, R. M., and Zebker, H. A., 1989, Mapping small elevation changes over large areas: Differential radar interferometry, Journal of Geophysical Research, **94**, 9183-9191.

Helm, D. C., 1975, One-dimensional simulation of aquifer system compaction near Pixley, California: 1. Constant parameters, Water Resources Research, 11, 3, 465-478, https://doi.org/10.1029/WR011i003p00465.

Helm, D. C., 1976, One-dimensional simulation of aquifer system compaction near Pixley, California: 2. Stress-dependent parameters, Water Resources Research, 12, 3, 375-391, https://doi.org/10.1029/WR012i003p00375.

Hofmann-Wellenhof, B., Lichtenegger, H. and Wasle, E., 2007, *GNSS-Global Navigation Satellite Systems: GPS, GLONASS, Galileo, and More* (Wien: Springer).

Hooper, A., 2008, A multi-temporal InSAR method incorporating both persistent scatterer and small baseline approaches, *Geophysical Research Letters*, **35**, L16302, 1-5.

Ireland, R. L., Poland, J. F., and Riley, F. S., 1984, Land Subsidence in the San Joaquin Valley, California, as of 1980, USGS Numbered Series 83-370, U. S. Geological Survey.

Kim, K. H., Liu, Z., Rodell, M., Beaudoing, H., Massoud, E., Kitchens, J., Dudek, M., Saylor, P., Corcoran, F., and Reager, J. T., 2020, An evaluation of remotely sensed and in situ data sufficiency for SGMA-scale groundwater studies in the Central Valley, California, Journal of the American Water Resources Association, 1-11, https://doi.org/10.1111/1752-1688.12898.

Lanari, R., Mora, O., Manunta, M., Mallorqui, J. J., Berardino, P, and Sansosti, E., 2004, A small baseline approach for investigating deformations on full-resolution differential SAR interferograms, *IEEE Transactions on Geoscience and Remote Sensing*, **42**, 1377-1386.

Lees, M., Knight, R., and Smith, R., 2022, Development and application of a 1D compaction model to understand 65 years of subsidence in the San Joaquin Valley, Water Resources Research, 58, e2021WR031390, https://doi.org/10.1029/2021WR031390.

Liu, P.-W., Famiglietti, J. S., Purdy, A. J., Adams, K. H., McEvoy, A. L., Reager, J. T., Bindlish, R., Wiese, D. N., David, C. H., and Rodell, M., 2022, Groundwater depletion in California's Central Valley accelerates during megadrought, Nature Communications, 13, 7825, 1-11, https://doi.org/10.1038/s41467-022-35582-x.

Massonnet, D., and Feigl, K., 1998, Radar interferometry and its application to changes in the Earth's surface, Reviews of Geophysics, **36**, 441-500.

Massonnet, D., Holzer, T., and Vadon, H., 1997, Land subsidence caused by the East Mesa geothermal field, California, observed using SAR interferometry, Geophysical Research Letters, **24**, 901-904.

Meade, R. H., 1964, Rearrangement of Particles During the Compaction of Clayey Sediments-Review, *U. S. Geological Survey Professional Paper,* **497-B**, Washington, D. C.

Neely, W. R., Borsa, A. A., Burney, J. A., Levy, M. C., Silverii, F., and Sneed, M., 2021, Characterization of groundwater recharge and flow in California's San Joaquin Valley from InSAR-observed surface deformation, Water Resources Research, 57, e2020WR028451. https://doi.org/10.1029/2020WR028451.

Samsonov, S., d'Oreye, N., 2012, Multidimensional time series analysis of ground deformation from multiple InSAR data sets applied to Virunga Volcanic Province. Geophysical Journal International, **191**, 1095-1108, http://dx.doi.org/10.1111/j.1365-246X.2012.05669.x.

Smith, R. and Knight, R., 2019, Modeling land subsidence using InSAR and airborne electromagnetic data, *Water Resources Research*, **55**, 2801-2819, https://doi.org/10.1029/2018WR024185.

Smith, R., Knight, R., Chen, J., Reeves, J. A., Zebker, H. A., Farr, T. G., and Lui. Z., 2017, Estimating permanent loos of groundwater storage in the Southern San Joaquin Valley, California, *Water Resources Research*, **53**, 5998-6017, https://doi.org/10.1002/2016WR019804.

Sneed, M., 2001, Hydraulic and Mechanical Properties Affecting Ground-Water Flow and Aquifer-System Compaction, San Joaquin Valley, California, *Open-File Report* **01-35**, U.S. Geological Survey, Sacramento, California.

Towill, Inc., 2021, *InSAR data accuracy for California Groundwater Basins CGPS data comparative analysis January 2015 to October 2020*. Retrieved from https://data.cnra.ca.gov/dataset/tre-altamira-insar-subsidence/resource/a1949b59-2435-4e5d-bb29-7a8d432454f5

Vasco, D. W., Harness, P., Pride, S., and Hoversten, M., 2017, Estimating fluid-induced stress change from observed deformation, Geophysical Journal International, **208**, 1623-1642.

Vasco, D. W., Farr, T. G., Jeanne, P., Doughty, C., and Nico, P., 2019, Satellite-based monitoring of groundwater depletion in California's Central Valley, *Nature Scientific Reports*, **9**, 16043, doi.org/10.1038/s41598-019-52371-7.

Vasco, D. W., Kim, K. H., Farr, T. G., Reager, J. T., Bekaert, D., Sangha, S. S., Rutqvist, J., and Beaudoing, H. K., 2022, Using Sentinel-1 and GRACE satellite data to monitor the hydrological variations within the Tulare Basin, California, *Scientific Reports,* **12**, 3867, doi.org/10.1038/s41598-022-07650-1.